Draft version September 26, 2014
Preprint typeset using LaTeX style emulateapj v. 5/2/11

arXiv:1409.7362v1 [astro-ph.GA] 25 Sep 2014

BINARIES TRAVELING THROUGH A GASEOUS MEDIUM: DYNAMICAL DRAG FORCES AND INTERNAL TORQUES

F. J. Sánchez-Salcedo
Instituto de Astronomía, Universidad Nacional Autónoma de México, Ciudad Universitaria, Apt. Postal 70 264, C.P. 04510, Mexico City, Mexico

and

Raul O. Chametla
Escuela Superior de Física y Matemáticas, Instituto Politécnico Nacional, UP Adolfo López Mateos, Mexico City, Mexico

Draft version September 26, 2014

ABSTRACT

Using time-dependent linear theory, we investigate the morphology of the gravitational wake induced by a binary, whose center of mass moves at velocity $\boldsymbol{V}_{\rm cm}$ against a uniform background of gas. For simplicity, we assume that the binary's components are on circular orbits about their common center of mass. The consequences of dynamical friction is twofold. First, gas dynamical friction may drag the binary's center of mass and cause the binary to migrate. Second, drag forces also induce a braking torque, which causes the orbits of the binary components to shrink. We compute the drag forces acting on one component of the binary due to the gravitational interaction with its own wake. We show that the dynamical friction force responsible to decelerate the binary's center of mass is smaller than it is in the point-mass case because of the loss of gravitational focusing. We show that the braking internal torque depends on the Mach numbers of each binary component about their center of mass, and also on the Mach number of the center of mass of the binary. In general, the internal torque decreases with increasing the velocity of the binary relative to the ambient gas cloud. However, this is not always the case. We also mention the relevance of our results on the period distribution of binaries.

Subject headings: binaries: general – black hole physics – hydrodynamics – ISM: general – waves

1. INTRODUCTION

Stars and black holes can accrete gas when they move through a gaseous medium (Bondi & Hoyle 1944). Gas accretion may shape the observed initial mass function of stars in young star-forming clusters (e.g., Bonnell et al. 2001; Maschberger et al. 2014). In addition to the aerodynamic drag force $\dot{M}V$ due to the accretion of gas, gravitational objects moving in a gas may also feel a drag or dynamical friction due to the gravitational interaction with its own-induced wake. There is a variety of astrophysical systems where gas dynamical friction plays an important role; e.g., gas dynamical friction is relevant to understand the orbital decay of common-envelope binary stars (Taam & Sandquist 2000; Nordhaus & Blackman 2006; Ricker & Taam 2008), the orbital decay of giant clumps in high-redshift galaxies (Immeli et al. 2004; Bournaud et al. 2007) or the shrinkage of the orbit of supermassive black holes in merging galaxies (e.g., Armitage & Natarajan 2002). Dynamical friction may affect the stellar dynamics in star clusters still embedded in their parent gas cloud, and/or a nuclear star cluster subject to major gas inflows (e.g., Davies et al. 2011). For instance, Chavarría et al. (2010) suggested that the mass segregation observed in two clusters of young stellar objects associated with massive star-forming regions in the Norma Spiral Arm could be explained by the migration of high-mass stars toward the center due to gaseous gravitational drag. Leigh et al. (2014) found that for the galactic nuclei and young star-forming regions considered in their study, the rate of mass segregation due to gas dynamical friction and accretion tends to be comparable to, albeit slightly smaller than, the rates from stellar two-body relaxation. Thus, gas damping can accelerate the rate of mass segregation.

In the work, we consider the problem of the orbital evolution of binaries embedded in gaseous media, e.g., in a cloud[1]. Dynamical friction will lead to a migration of the binary to the center of the cloud, producing mass segregation. In addition, dynamical interaction with the surrounding gas may produce a braking torque, which can lead to the extraction of energy and angular momentum from the binary (Kim et al. 2008; Stahler 2010). This torque tends to shrink the separation of the binary components, decreasing its orbital period around the center of mass of the binary. Korntreff et al. (2012) argued that during the time that the cluster is embedded in its natal gas ($\sim$ 1 Myr), the gas-induced orbital decay can reshape the period distribution in close systems (separations $\leq$ 30 AU). Moreover, they suggested that gas damping can catalyse the coalescence of star binaries, reducing the binary frequency.

One would expect that, since binary systems are, on average, more massive than single stars, they should present a more clear signature of mass segregation. Contrary to these expectations, de Grijs et al. (2013) and Li et al. (2013) showed evidence that the fraction of F-star binary systems in NGC 1818 increases with increasing distance from the cluster center. This could be indicative that either the dynamical friction is reduced in binary systems or, more likely,

[1] The evolution of binaries in stellar clusters due to the dynamical interactions with other stars has received considerable attention (e.g., Heggie 1975; Hills 1975; Hut 1983; Hut et al. 1992; Sigurdsson & Phinney 1993; Downing et al. 2010).

that they are observing hard binary systems (those with relatively high binding energies compared to the kinetic energy of bulk stellar population) that have survived and could have been hardened by dynamical encounters and by gas dynamical friction. Geller et al. (2013) found that, depending on the dynamical age of the cluster, the radial binary frequency distribution can either increase or decrease moving out radially from the cluster center, due to the combined effects of binary disruption and mass segregation.

Gas dynamical friction is also an important ingredient to understand the orbital decay of supermassive black holes at the center of galaxies (e.g., Armitage & Natarajan 2002; see Colpi 2014 for a review). It is believed that all galaxies with stellar spheroids possess a supermassive black hole. Thus, a merger of two galaxies leads to the formation of a supermassive black hole binary. If the timescale for coalescence of the black holes in the binary is longer than the time for succesive major mergers, then the galaxy may undergo a subsequent merger when the binary is still in place (Hoffman & Loeb 2007; Amaro-Seoane et al. 2010; Kulbarni & Loeb 2012). When a galaxy with a binary black hole merges with other galaxy that contains a central black hole, their black holes sink to the center of the merger product by dynamical friction, forming a triple black hole system. Therefore, it is interesting to understand the orbital decay of the center-of-mass of a binary black hole, due to dynamical friction, in the aftermath of a gas-rich merger. In addition to the orbital decay towards the center of the remnant, the binary is subject to loss of angular momentum about its center of mass, which means the separation between the components of the binary shrinks. Note that black hole binaries are expected to be surrounded by a rotating stellar and gaseous disk, resulting from the merger of the two parent disks. The associated drag depends on the differential rotation of the disk, its self-gravity and on the presence of resonances. Therefore, models that assume that the background is initially uniform and static cannot be applied to study the orbital decay of black hole binaries in the center of galaxies.

The orbital decay of a *single* perturber orbiting a gaseous cloud was studied numerically by Sánchez-Salcedo & Brandenburg (2001) and by Escala et al. (2004). Sánchez-Salcedo & Brandenburg (2001) found that an extension of the analytical formula derived by Ostriker (1999) for perturbers in rectilinear orbit and constant velocity in homogeneous media, is very successful in describing the orbital evolution. Escala et al. (2004) provided a fitting formula for the decay timescale of a massive perturber in a self-gravitating isothermal sphere. Cantó et al. (2013) derived a formula for the gravitational drag on a body moving in a vertically stratified medium of gas.

Kim, Kim & Sánchez-Salcedo (2008) considered an embedded-gas binary and derived the braking forces on each particle assuming that the two components of the binary are on circular orbits. Stahler (2010) studied the same problem but used a different approach to estimate the angular momentum exchange between the binary and the surrounding gas. In both calculations, it was assumed that the center-of-mass of the binary is at rest relative to the gaseous medium. The goal of this paper is to derive the drag forces and internal torques acting on a binary system in a more general situation in which the binary system is moving relative to the surrounding medium. We will see that the morphology of the wake, the drag force and the internal torques are modified, in a subtle manner, when the additional component of the center-of-mass velocity is included.

The paper is organized as follows. In Section 2, we present the mathematical framework to derive the gravitational wake excited by a binary system, using time-dependent linear perturbation theory. Estimates of the length scale at which the response of the gas departs from linearity are also discussed in Section 2. Since in linear theory the wake created by two perturbers is given by the simple superposition of the wakes of both perturbers, Section 3 describes the morphology of the resulting wake created by just one component of the binary. In Section 4, we evaluate the drag foce on the perturber due to its own wake. In Section 5 we provide estimates of the drag forces and internal torques in equal-mass binaries and outline how to determine the binary orbital evolution. Section 6 contains our conclusions.

2. FORMULATION OF THE PROBLEM, RELEVANT SCALES AND LINEAR THEORY

Consider a self-gravitating bound system whose center of mass moves at a velocity $\boldsymbol{V}_{\rm cm}$ relative to the gaseous background. The system could be a globular cluster orbiting the gaseous halo of a protogalaxy, a star cluster in the gaseous disk of a galaxy, or a binary star embedded in its progenitor cloud. To make the presentation readeable, we will consider the context of a binary system, but our approach and results are also valid and applicable in many other astrophysical scenarios.

2.1. *The orbit of one component of the binary*

We will compute the response of the gaseous medium to the gravitational potential created by a binary system that travels in a linear trajectory through an initially homogeneous medium with density and sound speed at infinity ρ_∞ and c_∞, respectively. As usual in studies of dynamical friction, we will assume that the orbital parameters of the binary are constant over time, i.e. we ignore the effect of the drag force on the orbit. Without loss of generality, we assume that the center of mass of the binary moves along the z-axis with velocity $V_{\rm cm}$, that is, $\boldsymbol{V}_{\rm cm}=V_{\rm cm}\hat{\boldsymbol{z}}$. In the binary frame, the two particles move in a plane; we will refer to it as the orbital plane.

Denote i as the inclination angle of the orbit (where i is assumed to lie between 0 and $\pi/2$), i.e. the angle between the vector perpendicular to the orbital plane and $\boldsymbol{V}_{\rm cm}$. When $i=0$, the orbital axis is aligned with the velocity of the center of mass and, thus, the binary moves face-on relative to the ambient medium. On the other hand, $i=\pi/2$ corresponds to an edge-on motion. Finally, we define a unit vector $\boldsymbol{e}_a$ along the intersection of the orbital plane with the reference plane $(\hat{\boldsymbol{x}},\hat{\boldsymbol{y}})$. We can always choose a system of reference where $\boldsymbol{e}_a$ is along the x-axis (that is, the longitude of the ascending node is zero).

For simplicity, we consider the case where the orbit of the binary is circular, and focus on the wake created by one of the components of the binary, with mass M (hereafter the perturber). We let R_p denote the radius of its orbit around

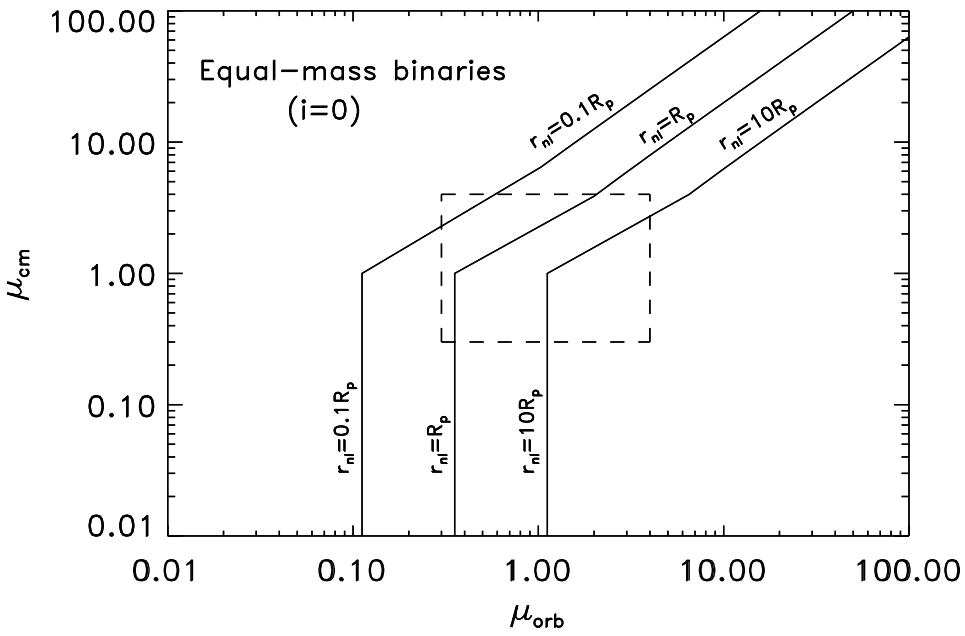

FIG. 1.— The contour lines show $r_{\rm nl}$, which is defined as the characteristic radius where the dynamics becomes nonlinear, in the plane $(\mu_{\rm orb}, \mu_{\rm cm})$, for an equal-mass binary with $i = 0$. Each curve indicates the different combinations of $\mu_{\rm orb}$ and $\mu_{\rm cm}$ that give the same $r_{\rm nl}$. The box indicates the parameter space explored in this paper.

the center of mass of the binary. In the frame of reference described above, the orbit is given by

$$x_p(t) = R_p \cos \Omega t, \tag{1}$$

$$y_p(t) = R_p \cos i \sin \Omega t, \tag{2}$$

$$z_p(t) = R_p \sin i \sin \Omega t + V_{\rm cm} t, \tag{3}$$

where we have assumed that, at $t = 0$, the perturber is at $x = R_p$, $y = 0$ and $z = 0$ and, in addition, for convention, $\Omega \geq 0$ and $V_{\rm cm} \geq 0$.

The gas will respond to the external gravitational potential created by the perturber, $\Phi_{\rm ext}$, which obeys the Poisson equation $\nabla^2 \Phi_{\rm ext} = 4\pi G \rho_{\rm ext}$, where $\rho_{\rm ext}$ is the density profile of the perturber. In our case:

$$\rho_{\rm ext}(\boldsymbol{r}, t) = M \delta(x - x_p(t)) \delta(y - y_p(t)) \delta(z - z_p(t)) \mathcal{H}(t), \tag{4}$$

where we are assuming that the perturber is a point-mass. Here $\mathcal{H}$ is an arbitrary function of t which may be used to describe how the perturber is introduced in the medium; $\mathcal{H} = 1$ corresponds to the stationary state, where the perturber is present since $t \to -\infty$. If $\mathcal{H}$ is the Heaviside function, $\mathcal{H}(t) = \Theta(t)$ the perturber is dropped suddently at $t = 0$, whereas if $\mathcal{H}(t) = (1 - \exp[-t/\tau])\Theta(t)$, the perturber is inserted adiabatically when τ is large enough. Ostriker (1999) noticed that for subsonic perturbers, the stationary solution does not capture all the physics of the problem.

It is useful to define the Mach number of the center of mass $\mu_{\rm cm} \equiv V_{\rm cm}/c_\infty$ and the orbital Mach number defined as $\mu_{\rm orb} \equiv V_{\rm orb}/c_\infty$, where $V_{\rm orb} \equiv \Omega R_p$. A model can thus be specified with three dimensionless parameters $(i, \mu_{\rm cm}, \mu_{\rm orb})$.

2.2. *Relevant length scales and applicability of the linear theory*

Discussions are more simple in the case where $i = 0$ because the modulus of the velocity of each perturber is constant. For $i > 0$, the relative velocity between one perturber and the ambient medium depends on the position along the orbit, which complicates the treatment. Therefore, we will focus on the face-on case ($i = 0$).

Consider for a moment the wake created by just one object of mass M that is forced to move in a helical motion without any other gravitational companion. If the perturber is a point-mass, there exists a neighbourhood around the body where the response of the gas becomes nonlinear. Let us denote $r_{\rm nl}$ the radius of this region. When the guiding center moves subsonically, $\mu_{\rm cm} < 1$, the response of the gas is nonlinear within the Bondi radius, r_B, defined as the distance at which the gravitational potential is comparable to the gas pressure, that is $r_{\rm nl} = r_B \equiv GM/c_\infty^2$. Now suppose that the motion of the guiding center is supersonic: $\mu_{\rm cm} > 1$. It is convenient to define the gravitational radius $r_{gc} \equiv GM/c_\infty^2(1 + \mu_{\rm cm}^2)$. If $r_{gc} \ll R_p$, then curvature effects of the orbit are not important and, therefore,

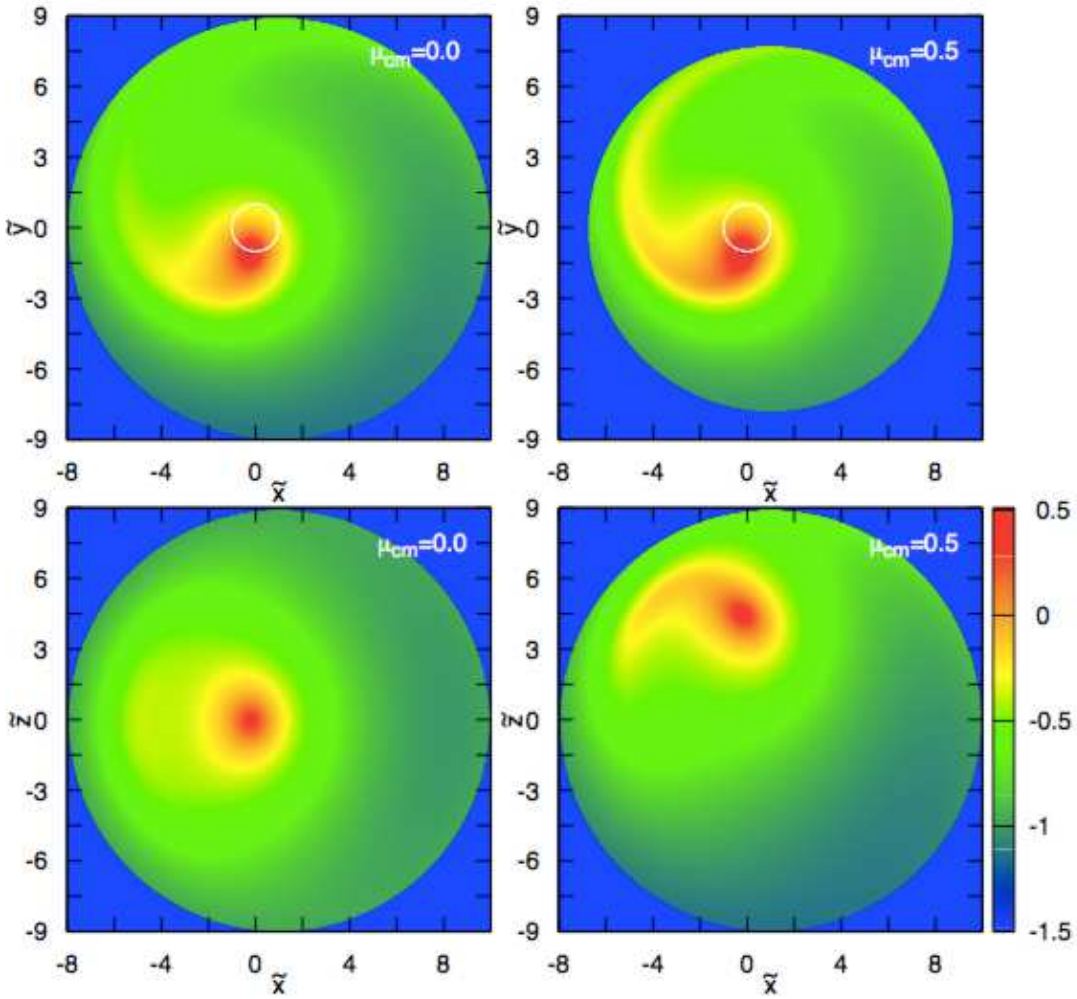

FIG. 2.— Color maps of the perturbed density $\mathcal{D}$ at $\tilde{t} = 9$ generated by a body in face-on motion with $\mu_{\rm orb} = 0.5$ and two different values of $\mu_{\rm cm}$. The top panels correspond to cutoffs through the (x, y)-plane at $\tilde{z} = 0$ (left) and $\tilde{z} = 4.5$ (right). These planes contain the perturber which can be distinguished as a very tiny black point. The white circles indicate the orbit of the perturber in each plane. The bottom panels show cutoffs through the plane $\tilde{y} = -0.5$. The perturber is located at $\tilde{r}_p = (-0.21, -0.98, 0)$ when $\mu_{\rm cm} = 0$, and at $(-0.21, -0.98, 4.5)$ when $\mu_{\rm cm} = 0.5$.

the response becomes nonlinear within the accretion radius[2], $r_{acc} = GM/c_\infty^2(1 + \mu_{\rm cm}^2 + \mu_{\rm orb}^2)$, which corresponds to the accretion radius of a body in rectilinear orbit with effective Mach number $(\mu_{\rm cm}^2 + \mu_{\rm orb}^2)^{1/2}$. If, on the other hand, $R_p \ll r_{gc}$, the orbit is so close that its size and the orbital velocity $V_{\rm orb}$ are both irrelevant. Under this condition, the problem is nonlinear at distances $\lesssim r_{gc}$ (i.e., $r_{\rm nl} = r_{gc}$). Since r_{acc} and r_{gc} are both proportional to M, $r_{\rm nl}$ also depends on M. Hence, $r_{\rm nl}$ can be arbitrarily small by decreasing the value of M.

In the presence of a companion, it is necessary to compute $r_{\rm nl}$ for each constituent of the binary, say $r_{\rm nl,1}$ and $r_{\rm nl,2}$. If $r_{\rm nl,1} + r_{\rm nl,2} < a$, where a is the separation of the binary, the nonlinear parts of the wakes do not intersect. Thus, the fluid is nonlinear in regions near each perturber with characteristic radii $r_{\rm nl,1}$ and $r_{\rm nl,2}$. For unequal-mass binaries with $M_1 \gg M_2$, the condition $r_{\rm nl,1}+r_{\rm nl,2} < a$ is satisfied either when $\mu_{\rm orb} < 1$ and $\mu_{\rm cm} < 1$, or when $\mu_{\rm cm}^2 > \max\{\mu_{\rm orb}^2 - 1, 1\}$.

Now consider an equal-mass binary, each component having mass M. The value of R_p and the orbital velocity are not independent but related through $V_{\rm orb}^2 = GM/(4R_p)$. Therefore, $R_p = GM/(4V_{\rm orb}^2)$. The Bondi radius of the binary, which has total mass $2M$, is $r_B = G(2M)/c_\infty^2 = 8\mu_{\rm orb}^2 R_p$. Consequently, if $\mu_{\rm orb} > 0.35$, then $r_B > R_p$. This means that if $\mu_{\rm cm} < 1$ and $\mu_{\rm orb} > 0.35$, the flow is in the nonlinear regime within a sphere of radius $\sim 8\mu_{\rm orb}^2 R_p$ around the binary.

If, on the other hand, the center of mass of an equal-mass binary moves supersonically at, say $\mu_{\rm cm} = 5$, then $r_{gc} = GM/c_\infty^2(1 + \mu_{\rm cm}^2) \simeq (1/6)\mu_{\rm orb}^2 R_p$. As a result, for $\mu_{\rm orb} \lesssim 1$, the flow becomes nonlinear in regions of size smaller than R_p near each component of the binary.

[2] The accretion radius is defined as the radius at which the blending of streamlines is important.

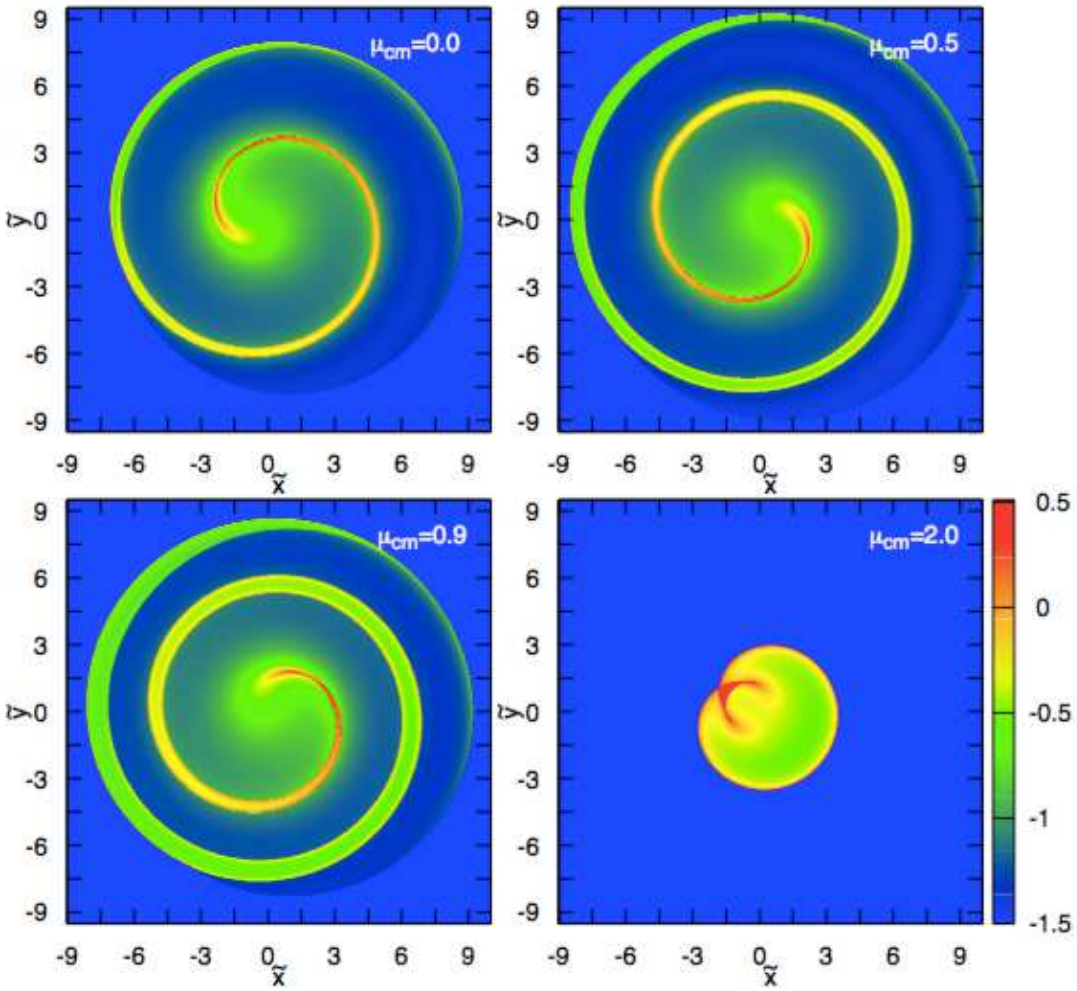

FIG. 3.— Density enhancement $\mathcal{D}$ created by a face-on perturber with $\mu_{\rm orb} = 2$, for different values of $\mu_{\rm cm}$, along a cutoff through the (x, y)-plane at $\tilde{z} = \tilde{z}_p - 4.5$, i.e., through planes situated at a vertical distance $4.5R_p$ behind the perturber. The time selected was $\tilde{t} = 9$ and thereby $\tilde{z}_p = \mu_{\rm cm} t = 9\mu_{\rm cm}$.

Following these arguments, we have constructed Figure 1, which shows contour lines of $r_{\rm nl}$ in the plane $(\mu_{\rm orb}, \mu_{\rm cm})$ for an equal-mass binary. In Section 3, we calculate the wake for $\mu_{\rm orb}$ and $\mu_{\rm cm}$ ranging between 0.3 and 4. As we see in Figure 1, $r_{\rm nl}$ may be as small as $0.1R_p$ in the limit case that $\mu_{\rm orb} \simeq 0.3$ and $\mu_{\rm cm} \simeq 4$. Therefore, *in equal-mass binaries* and for the parameters selected in this investigation, the linear approximation theory definitely breaks down at distances less than $\sim 0.1R_p$ from the perturber, or even at larger distances for other combinations of $(\mu_{\rm orb}, \mu_{\rm cm})$.

2.3. *The gravitational wake in linear theory*

In the previous section (§2.2), we have estimated the characteristic scales at which the flow becomes nonlinear. Far enough from the gravitational object, the perturbation is so small that it can be treated in the linear approximation. Combining the linearized equation of continuity and the linearized equation of motion, it is straightforward to find the differential equation for $\alpha(\boldsymbol{r}, t) \equiv (\rho - \rho_\infty)/\rho_\infty$, where $\rho(\boldsymbol{r}, t)$ is the gas density of the medium. The governing equation for $\alpha(\boldsymbol{r}, t)$ reads

$$\nabla^2\alpha - \frac{1}{c_\infty^2}\frac{\partial^2\alpha}{\partial t^2} = -\frac{4\pi G}{c_\infty^2}\rho_{\rm ext}(\boldsymbol{r}, t), \tag{5}$$

which corresponds to the inhomogeneous wave equation (e.g., Ostriker 1999). The formal solution of this equation is given by:

$$\alpha(\boldsymbol{r}, t) = \frac{G}{c_\infty^2}\int\int d^3\boldsymbol{r}'dt'\frac{\delta[t' - t + |\boldsymbol{r} - \boldsymbol{r}'|/c_\infty]\rho_{\rm ext}(\boldsymbol{r}', t')}{|\boldsymbol{r} - \boldsymbol{r}'|}. \tag{6}$$

For a point-mass perturber in a straight-line orbit (i.e. $\Omega = 0$), Equation (6) can be integrated analytically (Ostriker 1999). Here we will consider the case where the perturber follows a circular orbit around a guiding center (the binary's

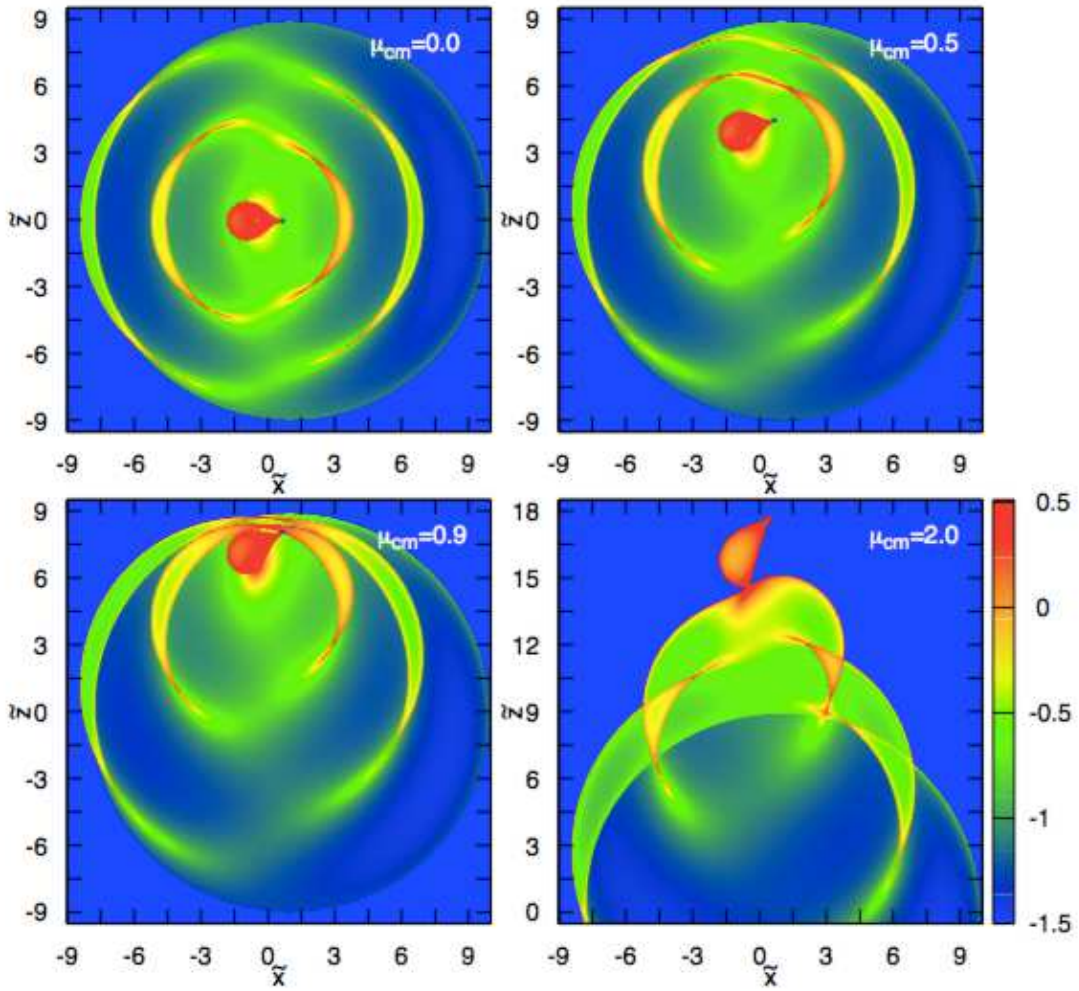

FIG. 4.— Same as Figure 3 but along a cutoff through the vertical plane $\tilde{y} = -0.8$, which passes through the location of the perturber at that time.

barycenter) which in turn moves on a straight-line trajectory (Eqs. 1-3). Substituting the expression for $\rho_{\rm ext}(\boldsymbol{r}, t)$ given in Eq. (4) into Equation (6) and integrating over x', y' and z', Equation (6) can be reduced to

$$\alpha(\boldsymbol{r}, t) = \frac{GM}{c_\infty^2 R_p} \int \frac{\delta[\varphi - \Omega t + \mu_{\rm orb}\tilde{d}(\varphi; \boldsymbol{r})]\mathcal{H}(\varphi/\Omega)}{\tilde{d}(\varphi; \boldsymbol{r})} d\varphi, \tag{7}$$

where we have used the new variable $\varphi \equiv \Omega t'$ (note that $\Omega \neq 0$) and

$$\tilde{d}(\varphi; \boldsymbol{r}) = \left[(\tilde{x} - \cos\varphi)^2 + (\tilde{y} - \cos i \sin\varphi)^2 + (\tilde{z} - \sin i \sin\varphi - \lambda\varphi)^2\right]^{1/2}, \tag{8}$$

where $\lambda \equiv \mu_{\rm cm}/\mu_{\rm orb}$. Remind that $\mu_{\rm orb} = \Omega R_p/c_\infty$. In the above equation (7) and throughout the paper, the tilde over one variable is used to indicate dimensionless quantities. The length scales are made dimensionless with R_p. Specifically, $\tilde{d} \equiv d/R_p$, $\tilde{x} \equiv x/R_p$ and so on.

In order to integrate Equation (7) over φ, we use the identity $\delta(g(\varphi)) = \sum \delta(\varphi - \varphi_j)/|g'(\varphi_j)|$, where φ_j are the roots of the function $g(\varphi)$. In our case, $g(\varphi) = \varphi - \Omega t + \mu_{\rm orb}\tilde{d}$, and its derivative is

$$g' \equiv \frac{dg}{d\varphi} = 1 + \frac{\mu_{\rm orb}}{\tilde{d}}\Big(\tilde{x}\sin\varphi - \tilde{y}\cos i\cos\varphi \tag{9}$$

$$-\tilde{z}(\sin i\cos\varphi + \lambda) + \lambda\sin i(\sin\varphi + \varphi\cos\varphi) + \lambda^2\varphi\Big).$$

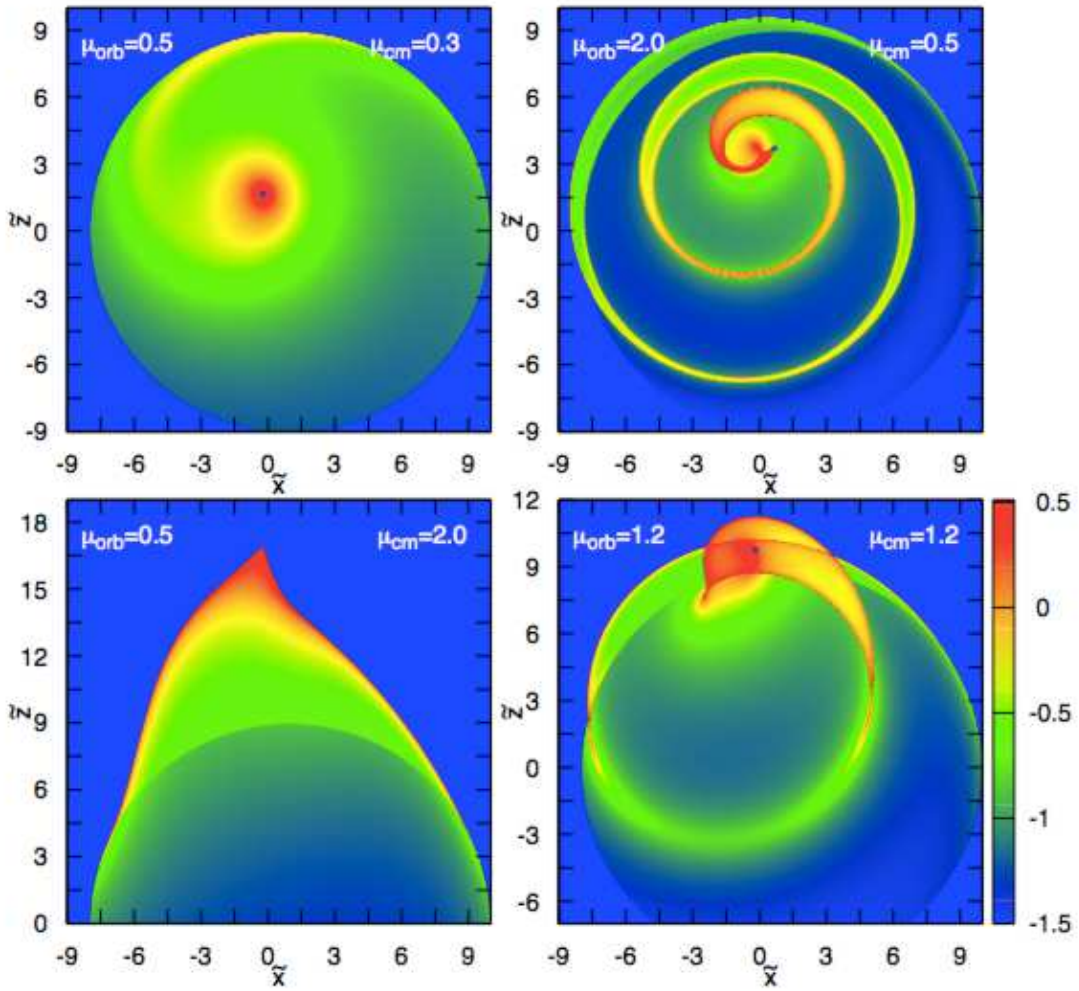

FIG. 5.— Distribution of the perturbed density $\mathcal{D}$ through the plane $y = 0$ for edge-on perturbers, at $\tilde{t} = 9$. The corresponding values of $\mu_{\rm cm}$ and $\mu_{\rm orb}$ are quoted at the right and left corners in each panel. Note that the trajectory of the perturber always lies in the plane $y = 0$.

The φ_j-values are the solutions of the following equation:

$$\mu_{\rm orb}\tilde{d}(\varphi;\boldsymbol{r}) = -(\varphi - \Omega t). \tag{10}$$

Evaluating the integral in Equation (7) and rearranging the terms, the perturbed density can be written as

$$\alpha(\boldsymbol{r},t) = \frac{GM}{c_\infty^2 R_p}\mathcal{D}(\boldsymbol{r}.t), \tag{11}$$

with

$$\mathcal{D}(\boldsymbol{r},t) = \sum_{\varphi_j} \frac{\mu_{\rm orb}}{|(1-\mu_{\rm cm}^2)\varphi_j - \Omega t - \mu_{\rm orb}^2[\tilde{x}\sin\varphi_j - \tilde{y}\cos i\cos\varphi_j - \tilde{z}(\sin i\cos\varphi_j + \lambda) + h(\varphi_j)]|}\mathcal{H}\left(\frac{\varphi_j}{\Omega}\right), \tag{12}$$

where

$$h(\varphi) = \lambda\sin i(\sin\varphi + \varphi\cos\varphi). \tag{13}$$

If we use R_p/c_∞ as the time unit, so that $\tilde{t} = t/(R_p/c_\infty)$, then $\Omega t = \Omega R_p\tilde{t}/c_\infty = \mu_{\rm orb}\tilde{t}$. Thus,

$$\mathcal{D}(\boldsymbol{r},t) = \sum_{\varphi_j} \frac{\mu_{\rm orb}}{|(1-\mu_{\rm cm}^2)\varphi_j - \mu_{\rm orb}\tilde{t} - \mu_{\rm orb}^2(\tilde{x}\sin\varphi_j - \tilde{y}\cos i\cos\varphi_j - \tilde{z}(\sin i\cos\varphi_j + \lambda) + h(\varphi_j)|}\mathcal{H}\left(\frac{\varphi_j}{\mu_{\rm orb}}\right), \tag{14}$$

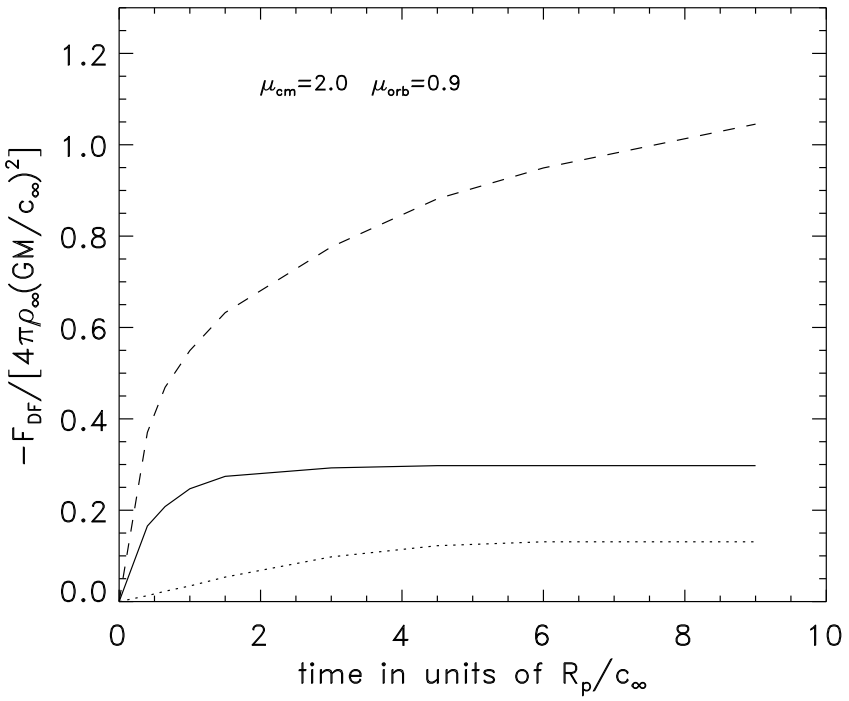

FIG. 6.— Temporal evolution of the z-component (dashed line), azimuthal component (solid line) and radial component (dotted line) of the dimensionless gravitational force for a single perturber in a face-on orbit with $\mu_{\rm cm} = 2$ and $\mu_{\rm orb} = 0.9$.

where the roots φ_j are the solutions of the equation:

$$\mu_{\rm orb}\tilde{d}_j = -(\varphi_j - \mu_{\rm orb}\tilde{t}). \tag{15}$$

These expressions can be simplified for face-on orbits (see Appendix A), and for edge-on orbits (see Appendix B). Kim & Kim (2007) studied the gravitational wake created by a perturber on a pure circular orbit. Appendix A also shows that Kim & Kim (2007) is recovered when $\mu_{\rm cm} = 0$.

The method to find the overdensity $\mathcal{D}(\boldsymbol{r}, t)$ is the same as described in Kim & Kim (2007). For the selected set of parameters $(i, \mu_{\rm cm}, \mu_{\rm orb})$, we construct a grid. At a given time $\tilde{t}$, we find numerically the roots of Equation (15) at each point of the grid $(\tilde{x}, \tilde{y}, \tilde{z})$, using the Newton-Raphson bisection method. Appendix C establishes the procedure to find the interval where the roots are located. Once the roots are found, we evaluate Equation (14) to find $\mathcal{D}(\boldsymbol{r}, t)$. One of the advantages of the semi-analytical approach is that $\mathcal{D}$ can be derived at the desired degree of accuracy. In addition, we can compute $\mathcal{D}$ at a time $\tilde{t}$ without the need to follow its evolution at all intermediate timesteps, as occurs when solving numerically a differential equation. Since the problem is transformed into an algebraic one, the density can be computed pixel-by-pixel, allowing to distribute the work in different processors or machines and thereby achieving very high-resolution in modest desktop computers.

We must stress again that the linear approximation does not capture correctly the structure of the flow in a neighbourhood of the body where $\mathcal{D} \geq c_\infty^2 R_p/(GM)$. Indeed, the structure of the flow in the non-linear region depends on whether the perturber is modeled as a perfect accretor or, on the opposite case, it is modeled as a non-divergent core gravitational potential.

3. THE WAKE INDUCED BY ONE COMPONENT

We specialize in the case where the perturber is introduced at $t = 0$. This corresponds to take $\mathcal{H}(t) = \Theta(t)$, where $\Theta(t)$ is the Heaviside step function, so that at $t < 0$ the medium is unperturbed. As a result, the summation in Equation (12) is only over positive roots (that is, only roots $\phi_j > 0$ contribute in Equation 12); in fact, $\mathcal{H}$ defines the region that sound waves launched at $t = 0$ have time to reach.

3.1. *Face-on case*

The temporal evolution of the wake created by a perturber in a pure circular orbit, i. e. $\mu_{\rm cm} = 0$, was described in full detail in Kim & Kim (2007). Due to the orbit curvature, the wake tail bends behind the perturber, creating spiral waves. As illustrated by Kim & Kim (2007), the thickness of the spiral waves and their level of winding depend on the orbital Mach number. Here we consider the case where $\boldsymbol{V}_{\rm cm}$ is nonzero.

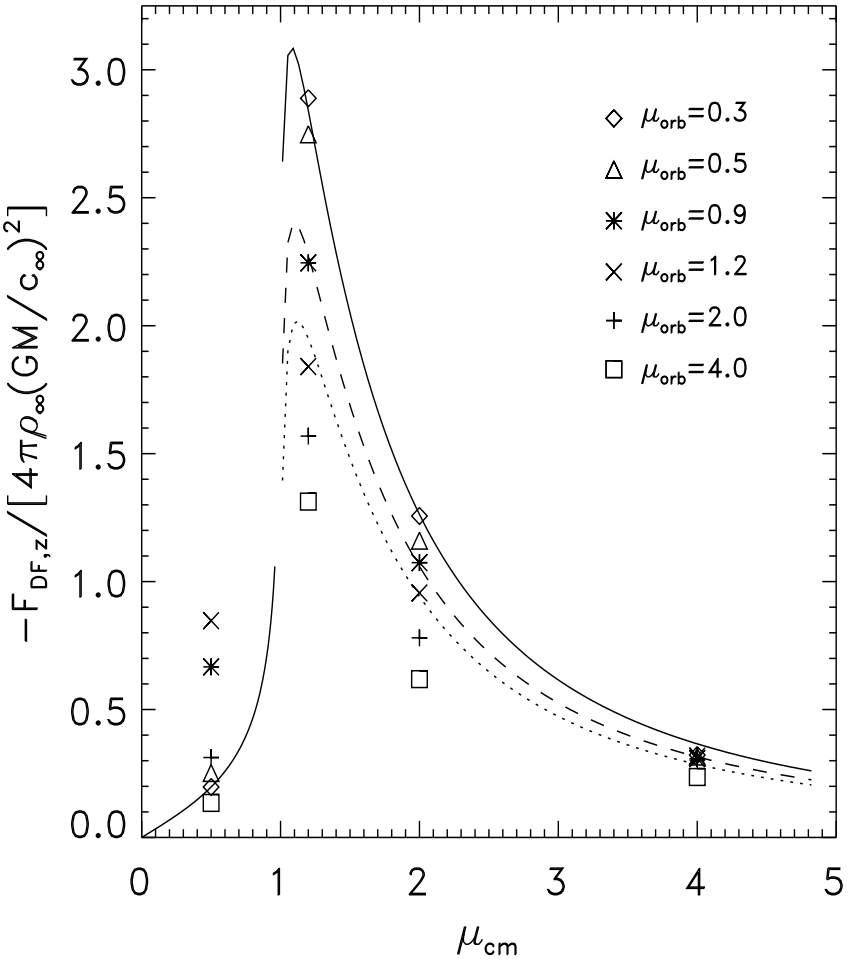

FIG. 7.— Vertical component (i.e. along the z-direction) of the dimensionless dynamical friction force for a gravitational object in the face-on case, as a function of $\mu_{\rm cm}$. The force was computed at $\tilde{t} = 9$. The curves draw the drag force as predicted by Ostriker's formula (1999) for a body moving at Mach number $\mu_{\rm cm}$ and adopting $r_{\rm inf} = r_{\rm min}$ (solid line), $r_{\rm inf} = 2.25 r_{\rm min} = 0.225 R_p$ (dashed line) and $r_{\rm inf} = 3.6 r_{\rm min} = 0.36 R_p$ (dotted line).

As said in Section 2.1, when $i = 0$, the orbital plane is perpendicular to $\boldsymbol{V}_{\rm cm}$ and the body describes a helical trajectory. It is interesting to compare the morphologies of the wakes created by perturbers in helical motion with those created by perturbers in circular orbit. Figure 2 shows the dimensionless density $\mathcal{D}$ at $\tilde{t} = 9$ (remind that the time unit is R_p/c_∞), when $\mu_{\rm orb} = 0.5$ for two values of $\mu_{\rm cm}$ (0 and 0.5). In both cases, the structure of the density wake presents a comma-like shape at the plane of the orbit, i.e. at $\tilde{z} = 0$ when $\mu_{\rm cm} = 0$ and at $\tilde{z} = 4.5$ when $\mu_{\rm cm} = 0.5$. Since the perturbers move subsonically ($\mu_{\rm orb}^2 + \mu_{\rm cm}^2 < 1$) in both cases, they always lie in the interior of the sonic sphere. Close enough to the perturber, at distances $\lesssim R_p$, a spheroidal envelope is formed around the perturber. At larger distances from the perturber, the disturbance forms a trailing one-armed spiral wave. This one-armed disturbance ends at the sonic sphere. The density maps in the (x, y)-plane that contains the perturber, look like qualitatively similar in both cases. In these maps, the perturbations are confined to a circle of radius $9R_p$ in the plane $\tilde{z} = 0$, and to a circle of radius $7.8R_p$ in the plane $\tilde{z} = 4.5$. These circles are obtained as the intersection of the sonic sphere, which is centered at the initial position of the perturber and has a radius of $9R_p$, with the planes $\tilde{z} = 0$ and $\tilde{z} = 4.5$, respectively. Interestingly, the density maps along vertical cuts are remarkably different. For $\mu_{\rm cm} = 0$, the density perturbation is symmetric with respect to the plane $z = 0$. This symmetry is broken when the perturber moves in the vertical direction; an elongated overdense structure can be observed in the cut along a vertical plane when $\mu_{\rm cm} = 0.5$.

The morphology of the wake changes dramatically for the perturber moves supersonically in the vertical direction. In the extreme case where $\mu_{\rm cm} > 1$ and $\mu_{\rm cm} \gg \mu_{\rm orb}$, a Mach cone is formed behind the perturber. However, because of the orbital motion, the axis of the Mach cone is not a straight line, as occurs in the rectilinear case, but follows a helicoidal curve. This occurs, for instance, for $\mu_{\rm orb} = 0.5$ and $\mu_{\rm cm} = 2$ (not shown).

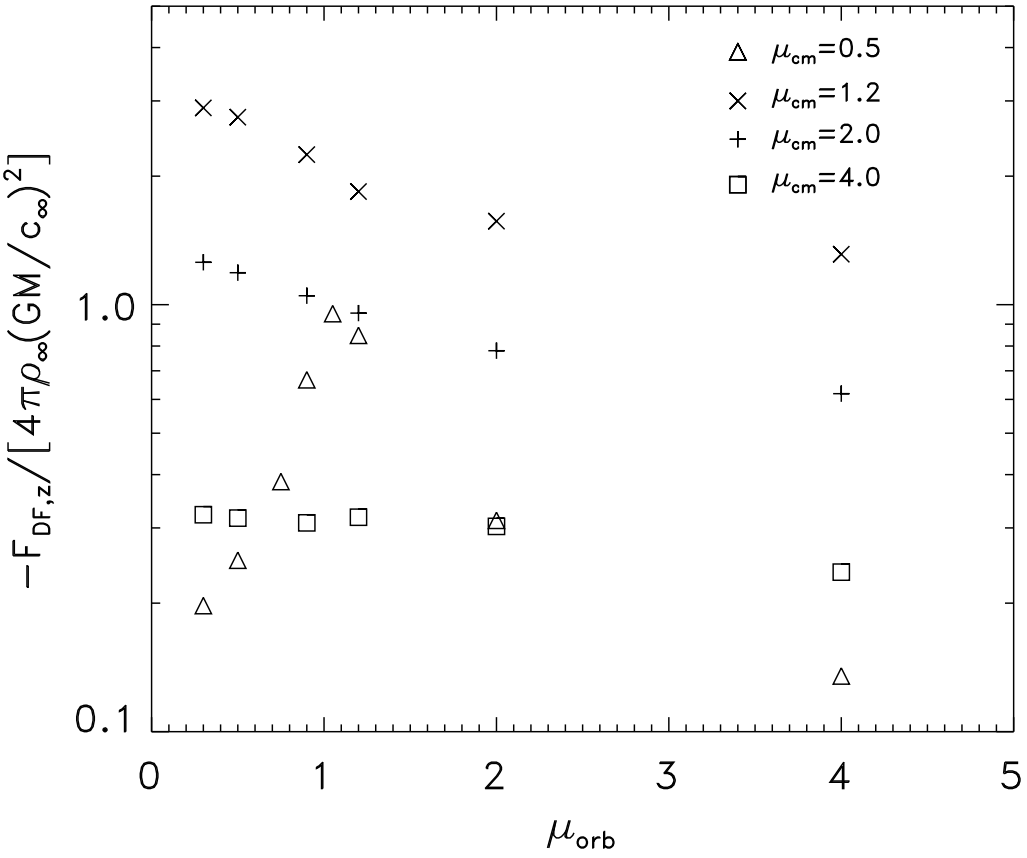

FIG. 8.— Vertical component (i.e. along the z-direction) of the dimensionless dynamical friction force for a gravitational object in the face-on case, as a function of $\mu_{\rm orb}$.

Now consider the case where the orbital motion is supersonic $\mu_{\rm orb} > 1$. For $\mu_{\rm cm} = 0$, the gravitational disturbance leads to the formation of an one-arm trailing tail that wraps around the perturber (see Kim & Kim 2007). The radial separation between two consecutive spiral crests is $2\pi R_p \mu_{\rm orb}^{-1}$. Figures 3 and 4 display the density disturbance for $\mu_{\rm orb} = 2$ and different $\mu_{\rm cm}$-values, along horizontal and vertical planes, respectively. When the perturber moves in the vertical direction, it is easy to identify the corresponding spiral wave fronts, more clearly in cuts along z =const planes, as long as $\mu_{\rm cm} < 1$. For supersonic motions in the vertical direction ($\mu_{\rm cm} > 1$), the morphology of the wake changes remarkably (see the fourth panel in Figure 4).

Figure 4 also shows the transversal structure of the spiral waves, which appear as long arcs (for $\mu_{\rm cm} < 1$). For $\mu_{\rm cm} \to 1$, the spiral wave fronts are bunched up closer together at $\mu_{\rm cm}\tilde{t} < \tilde{z} < \tilde{t}$ (i.e. at $V_{\rm cm}t < z < c_\infty t$ in physical units), especially for $\mu_{\rm cm} = 0.9$, because of the vertical motion of the perturber. Since we have selected vertical cuts that pass through the position of the perturber, we can see the Mach cone at the rear of the perturber, at distances $\sim R_p$ from it. Indeed, the Mach cone is formed because the perturber moves supersonically relative to the background.

When $\mu_{\rm cm} = \mu_{\rm orb} = 2$, the vertical distribution of the wake is very complex, with many overdense substructures. However, the overall density perturbation is confined within the large-scale rear Mach cone, defined by $R < R_p - (z - z_p)/(\mu_{\rm cm}^2 - 1)^{1/2}$, where $R^2 = x^2 + y^2$ is the cylindrical distance (see Appendix C). In fact, the perturber launches sound waves to the medium that necessarily must lie within the large-scale Mach cone to preserve the causality condition.

3.2. *Edge-on case*

The total Mach number $(\dot{x}_p^2 + \dot{y}_p^2 + \dot{z}_p^2)^{1/2}/c_\infty$ is constant along the orbit of the perturber only when $i = 0$. Otherwise, the total Mach number varies with the perturber's angular distance ϕ_p measured in the orbital plane, defined as $\phi_p \equiv \Omega t$ (see Eqs. 1-3). In this Section, we will focus on the edge-on orbit, $i = \pi/2$. In such a case, $y_p = 0$ at any time. The body moves in the plane $y = 0$ on an epicycle, which in turn moves along the z-axis. The maximum total Mach number is $\mu_{\rm cm} + \mu_{\rm orb}$ and occurs when $\phi_p = 2n\pi$ (with n an integer). The minimum total Mach number is $|\mu_{\rm cm} - \mu_{\rm orb}|$ at $\phi_p = (2n + 1)\pi$.

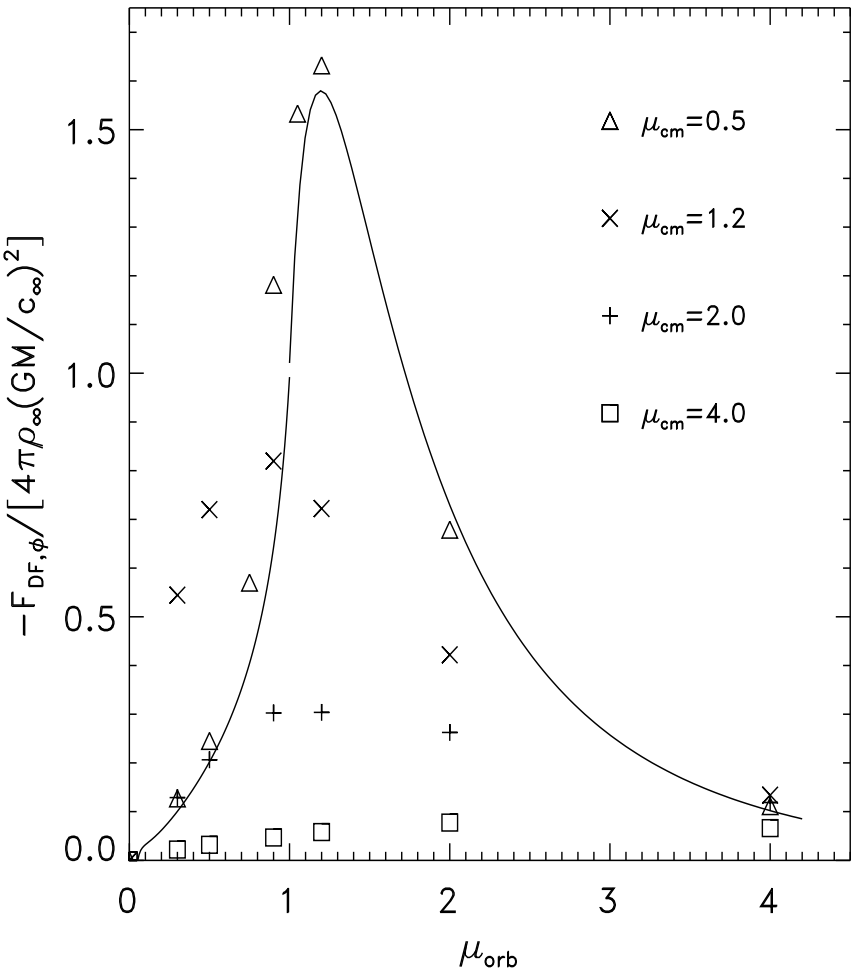

FIG. 9.— Azimuthal dynamical friction force, in dimensionless units, against $\mu_{\rm orb}$ in the face-on case. The force was computed at $\tilde{t} = 9$. At those times, the azimuthal component has practically reached the value of saturation. The solid line corresponds to the analytical fit derived by Kim & Kim (2007) for a pure circular orbit ($\mu_{\rm cm} = 0$).

Figure 5 shows the map of the density disturbance in the plane $y = 0$ for different combinations of $\mu_{\rm cm}$ and $\mu_{\rm orb}$. We see that when $\mu_{\rm cm} + \mu_{\rm orb} < 1$, that is, when the motion of the perturber is always subsonic, a comma-type wave, similar to that found in the face-on case with $\mu_{\rm cm}^2 + \mu_{\rm orb}^2 < 1$, is formed. It is remarkable that when $\mu_{\rm cm} = 0.5$ and $\mu_{\rm orb} = 2$, a spiral wave also emerges, as occurs in the face-on orbit, but now the thickness of the spiral wave clearly varies with z, being thicker at $z > z_p$ and thinner at $z < z_p$. This can be interpreted as follows. The spiral sound waves moves radially outwards at a velocity c_∞. Thus, the relative velocity between the perturber and the spiral waves in the radial direction varies with the azimuthal angle ϕ, from $(1 - \mu_{\rm cm})c_\infty$ at $\phi_p = \pi/2$, to $(1 + \mu_{\rm cm})c_\infty$, at $\phi_p = -\pi/2$. This asymmetry is responsible for the asymmetric thickness of the spiral waves found when $\mu_{\rm orb} > 1$ and $\mu_{\rm cm} < 1$.

When $\mu_{\rm cm} = 2$ and $\mu_{\rm orb} = 0.5$, the velocity of the perturber along the z-direction is always supersonic and, hence, the perturber is always at the apex of the deformed Mach cone. The overall structure of the wake resembles the wake of a supersonic body in the straight-line trajectory case but now the Mach cone is deformed because of the epicyclic motion and also because the total Mach number is not constant but varies between 1.5 and 2.5 along one epicycle.

The structure of the wake is very complex when $\mu_{\rm cm}$ and $\mu_{\rm orb}$ are both larger than 1 and comparable in magnitude. As an example, we show the case for $\mu_{\rm cm} = \mu_{\rm orb} = 1.2$. The total Mach number oscillates between 0 and 2.4. Density disturbances lag the perturber when it moves at the highest total Mach number (2.4 in this case), which occurs at $\phi_p = 2n\pi$. However, the perturber is swallowed by its own wake when it moves very subsonically at $\phi_p \approx (2n + 1)\pi$, creating a wake with a very irregular morphology.

4. THE DYNAMICAL FRICTION FORCE

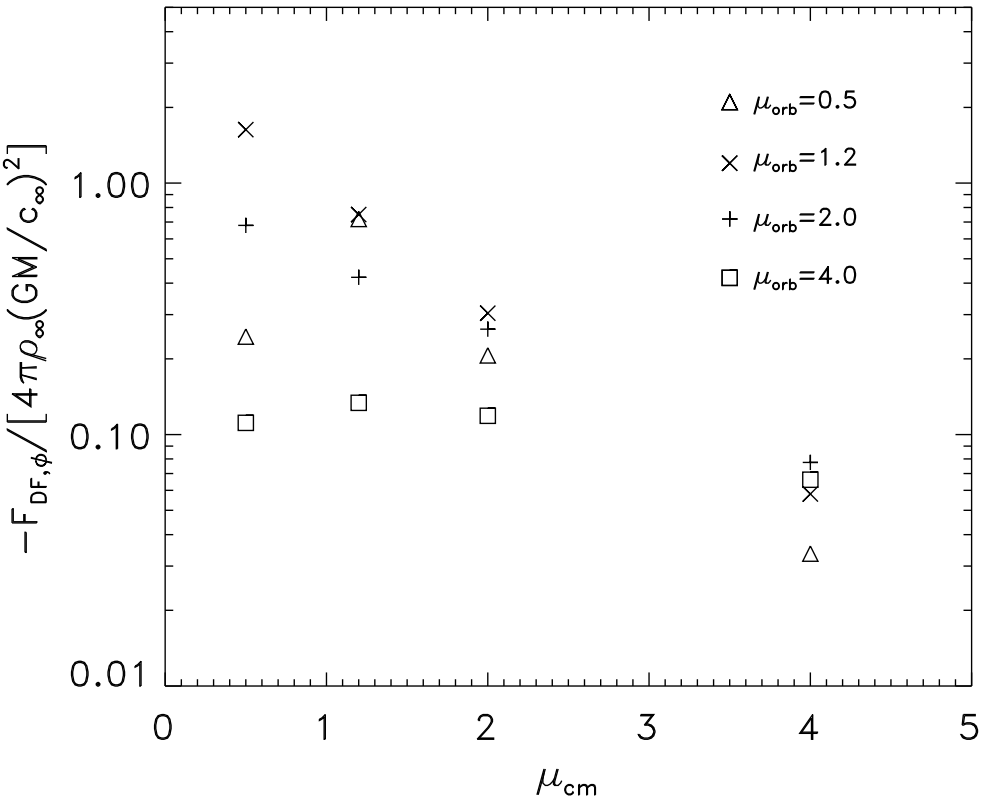

FIG. 10.— Azimuthal component of the drag force, as a function of $\mu_{\rm cm}$, for a body in face-on motion. It was computed at $\tilde{t} = 9$.

When a gravitational body moves through a gaseous medium, it experiences two forces, the aerodynamic force due to accretion, and the dynamical friction force, which arises from the gravitational attraction between the perturber and its wake.

In the case of a binary system, each component produces its own wake. Let the components of the binary have masses M and fM, where $f \leq 1$. In linear theory, the density disturbance in the wake is $\alpha = \alpha_1 + \alpha_2$, where α_1 and α_2 are the wakes induced by the perturbers with mass M and fM, respectively. Once the density wake $\alpha(\boldsymbol{r}, t)$ is known, the dynamical friction force exerted on the perturber of mass M can be computed as:

$$\boldsymbol{F}_{DF}^{(1)} = GM\rho_\infty \int \frac{\alpha(\boldsymbol{r}, t)(\boldsymbol{r} - \boldsymbol{r}_{p,1})}{|\boldsymbol{r} - \boldsymbol{r}_{p,1}|^3} d^3\boldsymbol{r}, \tag{16}$$

where $\boldsymbol{r}_{p,1}$ is the position vector of the perturber of mass M. Similarly, we can obtain $\boldsymbol{F}_{DF}^{(2)}$, the force acting on the mass fM.

Since in linear theory α diverges when $\boldsymbol{r} \to \boldsymbol{r}_{p,1}$, it is customary to introduce a minimum cut-off radius $r_{\rm min}$ to regularize the integral (16). Although there is some ambiguity in the definition of $r_{\rm min}$, in practice, it is taken as the characteristic distance from the body where the linear approximation fails (that is, $r_{\rm min} \approx r_{\rm nl}$). For instance, it is well-documented that for a compact object in supersonic rectilinear orbit, the linear formula for the drag force reproduces the drag force once the value provided for $r_{\rm min}$ is the accretion radius (e.g., Cantó et al. 2011; Bernal & Sánchez-Salcedo 2013).

4.1. *Components of the force*

The binary is subject to a net force $\boldsymbol{F}_{DF}^{(1)} + \boldsymbol{F}_{DF}^{(2)}$, hence

$$(1 + f)M \frac{d\boldsymbol{V}_{\rm cm}}{dt} = \boldsymbol{F}_{DF}^{(1)} + \boldsymbol{F}_{DF}^{(2)}. \tag{17}$$

One expects that the net force will tend to decelerate the binary center of mass, which we have assumed that moves in the z-direction. For $i = 0$ and $f = 1$, $\boldsymbol{F}_{DF}^{(1)} + \boldsymbol{F}_{DF}^{(2)}$ points in the z-direction because of the symmetry of the problem.

As we have seen in Section 3, binary systems induce spiral waves in the ambient medium, which are suitable to produce a braking torque on the binary. The angular momentum of the binary about the center of mass, $\boldsymbol{L}$, evolves according to

$$\frac{d\boldsymbol{L}}{dt} = \boldsymbol{r}_{p,1} \times \boldsymbol{F}_{DF}^{(1)} + \boldsymbol{r}_{p,2} \times \boldsymbol{F}_{DF}^{(2)}. \tag{18}$$

Torques perpendicular to $\boldsymbol{L}$ cause the binary's orbital plane to precess. Here we are interested in the change of L^2 due to the gravitational interaction with the surrounding gas. If the binary gains angular momentum it widens, whereas it shrinks when it loses angular momentum. The variation of L with time is given by

$$\frac{dL^2}{dt} = 2[\boldsymbol{F}_{DF}^{(1)} \cdot (\boldsymbol{L} \times \boldsymbol{r}_{p,1}) + \boldsymbol{F}_{DF}^{(2)} \cdot (\boldsymbol{L} \times \boldsymbol{r}_{p,2})]. \tag{19}$$

If the two components of the binary are on circular orbits about their common center of mass[3], $\boldsymbol{L}$ is perpendicular to both $\boldsymbol{r}_{p,1}$ and $\boldsymbol{r}_{p,2}$. Hence, we can write $\boldsymbol{L} \times \boldsymbol{r}_{p,1} = R_{p,1} L \hat{\boldsymbol{e}}_{\phi,1}$, where $\hat{\boldsymbol{e}}_{\phi,1}$ is the vector perpendicular to both $\boldsymbol{L}$ and $\boldsymbol{r}_{p,1}$. We arrive at

$$\frac{dL}{dt} = R_{p,1} F_{DF,\phi}^{(1)} + R_{p,2} F_{DF,\phi}^{(2)}. \tag{20}$$

In order to easy the comparison with previous studies that deal with a single perturber, we provide first $\boldsymbol{F}_{DF}$, defined as the force exerted on the perturber of mass M by its own induced wake $\mathcal{D}_1$:

$$\boldsymbol{F}_{DF} \equiv \frac{(GM)^2 \rho_\infty}{c_\infty^2} \int \frac{\mathcal{D}_1(\boldsymbol{r}, t)(\tilde{\boldsymbol{r}} - \hat{\boldsymbol{r}}_{p,1})}{|\tilde{\boldsymbol{r}} - \hat{\boldsymbol{r}}_{p,1}|^3} d^3\tilde{\boldsymbol{r}}. \tag{21}$$

To simplify the notation, the subscript 1 to denote perturber's orbital radius will be dropped out: $R_{p,1} \to R_p$.

In order to evaluate the integral in Eq. (21), the computational domain was divided in several blocks, along the wake, with different degree of refinement; the block containing the perturber has the highest resolution (about 200-400 zones per R_p). The resolution of the blocks was degraded depending on the distance to the perturber. For the most demanding calculations, those having large Mach numbers or Mach numbers close to unity, 8 blocks were used. For supersonic perturbers, we introduced a small softening of ~ 2 pixels at discontinuities where $\mathcal{D}$ diverges, in order to suppress numerical noise. Note that linear theory predicts those kind of density discontinuities even in the linear trajectory case (e.g., Ostriker 1999).

4.2. *Drag force induced by its own wake: face-on orbits*

In this Section, we consider one component of the binary and report the drag force due to its own wake $\boldsymbol{F}_{DF}$ in the face-on case ($i = 0$). $\boldsymbol{F}_{DF}$ will depend on three parameters: $\mu_{\rm orb}, \mu_{\rm cm}$ and the adopted value for $r_{\rm min}$. As already discussed, $r_{\rm min}$ is connected with the different gravitational spheres of influence defined in Section 2.2. For practical purposes, the $r_{\rm min}$ value must be calculated in each particular situation. For a circular binary with masses M and fM in a medium with sound speed c_∞, the cut-off radius is entirely determined by f, c_∞, $\mu_{\rm orb}$ and $\mu_{\rm cm}$.

In order to isolate the effect of each three parameter $\mu_{\rm orb}$, $\mu_{\rm cm}$ and $r_{\rm min}$, we first study the dependence of the drag force on the Mach numbers using a fixed value of $r_{\rm min}$ (Section 4.2.1). This is customary in studies of dynamical friction and will help us to obtain a more complete understanding on how the presence of epicyclic motions modify the nature of the force. We will take $r_{\rm min} = 0.1 R_p$ to facilitate comparison with Kim & Kim (2007). The dependence of the drag force on $r_{\rm min}$ is discussed in Section 4.2.2.

4.2.1. *Drag forces: Dependence on $\mu_{\rm cm}$ and $\mu_{\rm orb}$*

Figure 6 shows the components of $\boldsymbol{F}_{DF}$, as functions of time, for $\mu_{\rm cm} = 2$ and $\mu_{\rm orb} = 0.9$ (remind that, unless otherwise state, we use $r_{\rm min} = 0.1 R_p$). Remind that $F_{DF,\phi}$ is the azimuthal component and $F_{DF,R}$ the radial component in the frame of the binary, with its center of mass situated at the origin. We see that $F_{DF,\phi}$ and $F_{DF,R}$ both converge to their respective steady-state values, but $F_{DF,z}$ increases in time logarithmically. Kim & Kim (2007) already found that for a perturber on a pure circular orbit ($\mu_{\rm cm} = 0$), the drag components $F_{DF,\phi}$ and $F_{DF,R}$ converge to their respective steady-state values within a timescale $\sim 2R_p/c_\infty$ for subsonic perturbers or within $\sim 2\pi R_p/V_{\rm orb}$ for supersonic perturbers. This means that the temporal behaviour of $F_{DF,\phi}$ and $F_{DF,R}$ is similar to the case of pure circular orbit, whereas the temporal behaviour of $F_{DF,z}$ is similar to the case of rectilinear orbit. The reason is clear: in the z-direction, the Mach cone trailing the perturber is continuously growing along the z-direction because $\mu_{\rm cm} > 1$. In the ϕ-direction, the curvature of the orbit produces the saturation of $F_{DF,\phi}$ and $F_{DF,R}$. When $\mu_{\rm cm} < 1$, the three components of $\boldsymbol{F}_{DF}$ asymptotically approach constant values with time.

Figure 7 presents the vertical drag component, $F_{DF,z}$, at $\tilde{t} = 9$ as a function of $\mu_{\rm cm}$ for different values of $\mu_{\rm orb}$. In order to quantify the effect of the orbital motion on $F_{DF,z}$, we have also plotted $F_{DF,z}$ for a body with $\mu_{\rm orb} = 0$:

$$F_{DF,z} = \frac{4\pi\rho_\infty (GM)^2}{c_\infty^2} \frac{1}{\mu_{\rm cm}^2} \left[\frac{1}{2} \ln\left(\frac{1+\mu_{\rm cm}}{1-\mu_{\rm cm}} \right) - \mu_{\rm cm} \right], \tag{22}$$

[3] As usual, we assume that the change of the orbital parameters of the binary due to the drag force and internal torques on the binary occurs on a timescale much longer than any other relevant timescale. So, it is a good approximation to consider unperturbed orbits.

if $\mu_{\rm cm}=0$, $\mu_{\rm cm}<1$ and $t>r_{\rm inf}/[c_\infty(1-\mu_{\rm cm})]$, and

$$F_{DF,z}=\frac{4\pi\rho_\infty(GM)^2}{c_\infty^2}\frac{1}{\mu_{\rm cm}^2}\left[\frac{1}{2}\ln(1-\mu_{\rm cm}^{-2})+\ln\left(\frac{\mu_{\rm cm}c_\infty t}{r_{\rm inf}}\right)\right], \tag{23}$$

if $\mu_{\rm cm}=0$, $\mu_{\rm cm}>1$ and $t>r_{\rm inf}/[c_\infty(\mu_{\rm cm}-1)]$ (Ostriker 1999). Here $r_{\rm inf}$ is the minimum cut-off radius for a particle in a straight-line orbit. This implies that when $\mu_{\rm orb}=0$, $r_{\rm inf}$ must be equal to $r_{\rm min}$. In fact, Figure 7 illustrates this situation; for $\mu_{\rm orb}<0.5$, Ostriker's formula with $r_{\rm inf}=r_{\rm min}$ provides reasonably good estimates of the vertical drag force.

Figures 7 and 8 show that, at a fixed value of $\mu_{\rm cm}$ greater than 1, $F_{DF,z}$ decreases when $\mu_{\rm orb}$ increases. The physical reason is that the orbital motion around the center of mass, induces a loss of gravitational focusing in the z-direction. If we wish to continue using Ostriker's formula, we must use a larger effective $r_{\rm inf}$. For instance, Ostriker's formula provides the correct value of $F_{DF,z}$, for $\mu_{\rm orb}=0.9$ and $\mu_{\rm cm}>1$, when $r_{\rm inf}=2.25r_{\rm min}$ is used. For $\mu_{\rm orb}=1.2$, one requires $r_{\rm inf}=3.36r_{\rm min}$.

In Figure 8, we see that at a fixed $\mu_{\rm cm}=0.5$, the steady-state vertical component $F_{DF,z}$, as a function of $\mu_{\rm orb}$, has its peak at around $\mu_{\rm orb}=1.2$, being its magnitude almost 4 times larger than it is for $\mu_{\rm orb}=0.3$ or $\mu_{\rm orb}=4$. Beyond $\mu_{\rm orb}=1.2$, $F_{DF,z}$ decreases rapidly with $\mu_{\rm orb}$.

The azimuthal component of the force, $F_{DF,\phi}$, which is responsible for the loss of orbital angular momentum, is shown in Figures 9 and 10. For $\mu_{\rm cm}=0$, our values of $F_{DF,\phi}$ match those derived by Kim & Kim (2007). At $\mu_{\rm cm}=0.5$, $F_{DF,\phi}$ is slightly shifted as compared to the values for $\mu_{\rm cm}=0$. Therefore, the analytical formula in Kim & Kim (2007) provides good estimates of $F_{DF,\phi}$ as long as $\mu_{\rm cm}<0.5$. In general, Kim & Kim (2007) formula is satisfactory when $\mu_{\rm orb}\gg\mu_{\rm cm}$.

Figure 9 shows the functional relationship between $F_{DF,\phi}$ and $\mu_{\rm orb}$ for different values of $\mu_{\rm cm}$. We see that, in the range $0<\mu_{\rm orb}<2.5$, the $F_{DF,\phi}$-$\mu_{\rm orb}$ relationship derived at $\mu_{\rm cm}=1.2$ is different from the relationship found for $\mu_{\rm cm}=0$. The maximum of $F_{DF,\phi}$ for $\mu_{\rm cm}=1.2$ occurs at orbital mach numbers around 0.9 and its value is a factor of 2 smaller than the corresponding peak value of $F_{DF,\phi}$ vs. $\mu_{\rm orb}$ at $\mu_{\rm cm}=0$.

For subsonic orbital Mach numbers ($\mu_{\rm orb}<1$), $F_{DF,\phi}$ is significantly larger for $\mu_{\rm cm}=1.2$ than it is for $\mu_{\rm cm}=0$ (see Figure 9). In particular, $F_{DF,\phi}$ for $\mu_{\rm orb}=0.5$ and $\mu_{\rm cm}=1.2$ is a factor of 3.5 larger than it is for $\mu_{\rm orb}=0.5$ and $\mu_{\rm cm}=0$. The reason is that the high front-back symmetry of the wake near the body (say, at distances $\leq R_p$), when $\mu_{\rm cm}=0$ and $\mu_{\rm orb}=0.5$, is broken when the perturber moves supersonically (as $\mu_{\rm cm}=1.2$). Therefore, it is misleading to think that the presence of translational motions always reduces $F_{DF,\phi}$. For $\mu_{\rm orb}<1$, $F_{DF,\phi}$ with $\mu_{\rm cm}=2$ is very similar to $F_{DF,\phi}$ for $\mu_{\rm cm}=0$.

When the orbital and the vertical Mach numbers are similar and supersonic, $\mu_{\rm cm}\simeq\mu_{\rm orb}>1$, the azimuthal component of the drag force is reduced by a factor of 2 as compared to the case when $\mu_{\rm cm}=0$. As expected, the largest suppression in $F_{DF,\phi}$ occurs at the largest $\mu_{\rm cm}$. For $\mu_{\rm orb}=1.2$ and $\mu_{\rm cm}=4$, $F_{DF,\phi}$ is a factor of 30 smaller than it is for $\mu_{\rm orb}=1.2$ and $\mu_{\rm cm}=0$.

Figure 10 shows $F_{DF,\phi}$ as a function of $\mu_{\rm cm}$ for different values of $\mu_{\rm orb}$. When $\mu_{\rm orb}=4$, $F_{DF,\phi}$ only varies about 30% in the range $0<\mu_{\rm cm}<4$. However, when $\mu_{\rm orb}=1.2-2$, $F_{DF,\phi}$ decreases monotonically with $\mu_{\rm cm}$ by a factor ≥ 10 in the range $0<\mu_{\rm cm}<4$.

4.2.2. *Drag forces: Dependence on $r_{\rm min}$*

Figure 11 shows the vertical and azimuthal components of the drag force for different values of $r_{\rm min}$, and for some combinations of $\mu_{\rm cm}$ and $\mu_{\rm orb}$. When both motions are subsonic, the drag force is not sensitive to the value of $r_{\rm min}$ as it varies from $0.1R_p$ to $1R_p$. Physically, this means that the wake within R_p does not contribute to the drag because of its back-front symmetry.

It is useful to define ΔF_z as the contribution to the (dimensionless) drag force by the portion of the wake lying between a distance $0.1R_p$ and a distance R_p from the perturber. For a supersonic perturber moving in a straight-line with Mach number μ, $\Delta F_z=\mu^{-2}\ln 10$. This implies that $\Delta F_z=1.6$ for $\mu=1.2$, and $\Delta F_z=0.57$ at $\mu=2$. In the case of helical motion with $\mu_{\rm cm}=2$ and $\mu_{\rm orb}=0.5$, we found that $\Delta F_z=0.48$ (see Fig. 11), which is slightly smaller than for the rectilinear orbit. However, for $\mu_{\rm cm}=1.2$ and $\mu_{\rm orb}=1.2$, we found that $\Delta F_z=0.55$ if the motion is helical. This value is much less than the value for rectilinear orbit (1.6) because the gravitational focusing of mass is reduced at distances $\sim R_p$ from the perturber due to the orbital (epicyclic) motion.

The dependence of $F_{DF,\phi}$ on $r_{\rm min}$ is shown in the lower panel of Fig. 11. We see that the slope of these curves increases with $\mu_{\rm orb}$. Still, even when the orbital motion is subsonic, $F_{DF,\phi}$ is sensitive to $r_{\rm min}$ if the translational motion is large enough. For instance, for $\mu_{\rm orb}=0.5$ and $\mu_{\rm cm}=2$, $F_{DF,\phi}$ decreases a factor of 2.4 if $r_{\rm min}=R_p$, instead of $0.1R_p$, is used. It is noteworthy that for $\mu_{\rm orb}=2$ (and $\mu_{\rm cm}=0.5$), $F_{DF,\phi}$ decreases by a factor of ~ 7 on the interval of $r_{\rm min}$ under consideration. This signifies that most of the azimuthal component of the drag force is caused by the gravitational attraction between the perturber and gas within a volume of radius $\sim R_p$ surrounding the perturber. Therefore, $F_{DF,\phi}$ is very sensitive to the adopted value of $r_{\rm min}$.

The strong suppression of $F_{DF,\phi}$ with $r_{\rm min}$ at $\mu_{\rm orb}\gtrsim 2$ and $\mu_{\rm cm}\lesssim 1$ has profound implications when dealing with binary systems. To illustrate this issue, consider an equal-mass binary. According to Figure 1, $r_{\rm min}\gtrsim 10R_p$ at the abovementioned Mach numbers. Unfortunately, we were unable to obtain accurate inferences of $F_{DF,\phi}$ when using $r_{\rm min}>10R_p$ because the result is severely polluted by numerical noise. Nevertheless, a rough extrapolation of the solid line in Figure 11 at $r_{\rm min}=10R_p$ indicates that the contribution of the "linear" part of the wake to the azimuthal

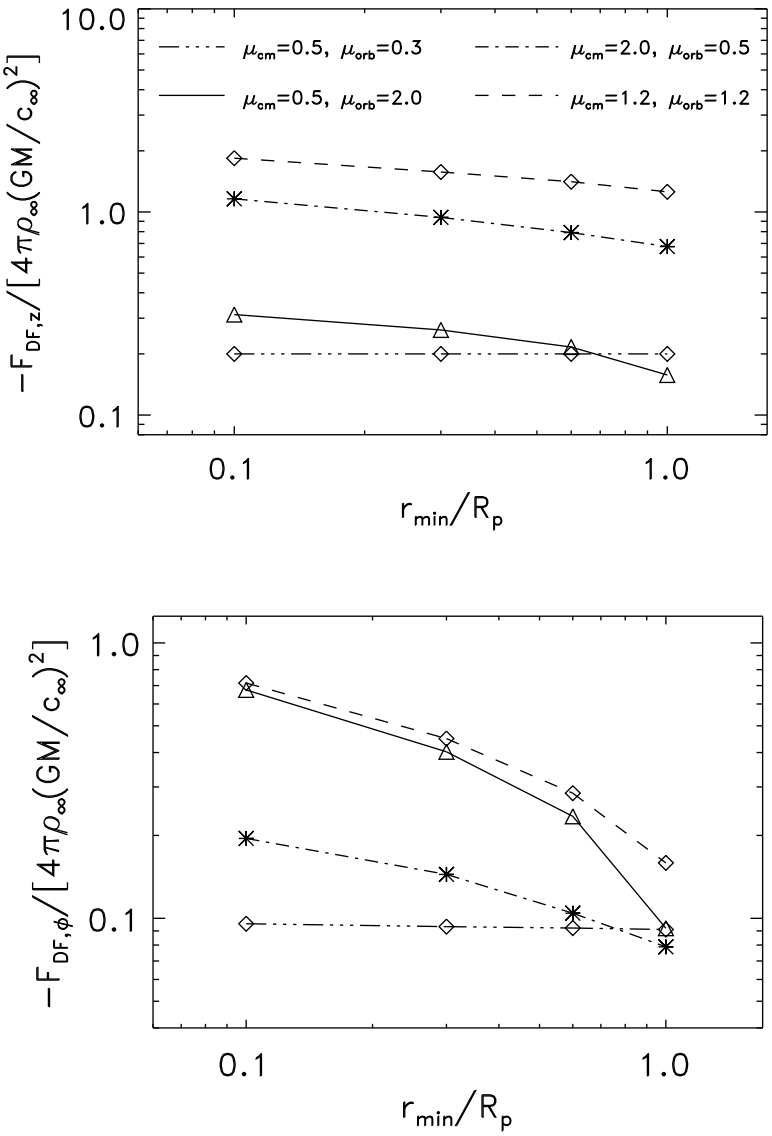

FIG. 11.— Dependence of the z-component (upper panel) and azimuthal component (lower panel) of the drag force on the adopted value of $r_{\rm min}$, for four different combinations of $\mu_{\rm cm}$ and $\mu_{\rm orb}$. The forces were calculated at $\tilde{t} = 9$.

drag force, is very small. Under these circumstances, it is possible that the contribution of the nonlinear part of the wake dominates the value of $F_{DF,\phi}$. This possibility can only be tested by using fully hydrodynamical simulations.

4.3. *Drag force induced by its own wake: edge-on orbits*

Consider now the extreme case $i = \pi/2$, where the orbital plane lies in the $x - z$ plane and the center of mass moves along the z-direction. By symmetry, $F_{DF,y} = 0$. Thus, the drag force lies within the plane $y = 0$. In this case, the components $F_{DF,z}$ and $F_{DF,\phi}$ will depend on the perturber's azimuthal angle ϕ_p (remind that $\phi_p \equiv \Omega t$). Figure 12 shows $F_{DF,z}$ and $F_{DF,\phi}$ along one orbital time $t_{\rm orb}$, which is $2\pi/\Omega = 2\pi R_p/(c_\infty \mu_{\rm orb})$. We have used $r_{\rm min} = 0.1R_p$. The reference time $\tilde{t} = 9$, corresponds to 0.43 orbits when $\mu_{\rm orb} = 0.3$, to 2.86 orbits when $\mu_{\rm orb} = 2$, to 0.72 orbits when $\mu_{\rm orb} = 0.5$ and to 1.72 orbits when $\mu_{\rm orb} = 1.2$.

When $\mu_{\rm cm} = 0.5$ and $\mu_{\rm orb} = 0.3$, the two components $F_{DF,z}$ and $F_{DF,\phi}$, vary approximately in phase. They take their maximum absolute value at $\phi_p = 2\pi$, i.e. when an orbit is completed and the instantaneous total Mach number is 0.8, whereas the minimum absolute values occur at $\phi_p = \pi$, when the total Mach number is 0.2. The mean values averaged over one orbital time (more specifically, between 0.2 and 1.2 orbits) are $\langle F_{DF,z}\rangle = -0.25$ and $\langle F_{DF,\phi}\rangle = -0.18$ in dimensionless units. These values are very similar to those found in the face-on case.

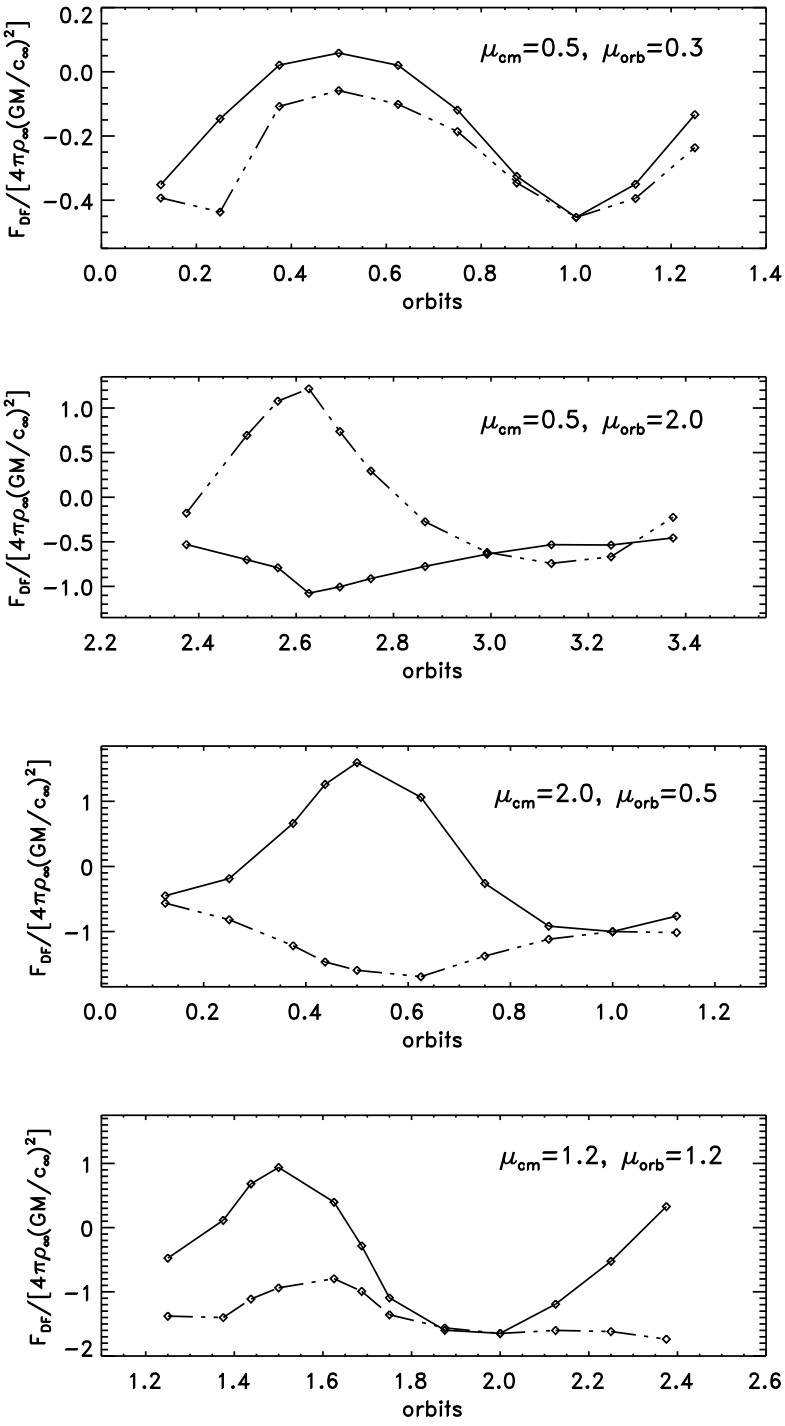

FIG. 12.— Azimuthal component $F_{DF,\phi}$ (solid lines) and z-component (dash-dotted line) of the drag force for an edge-on perturber ($i = 90°$) along approximately one orbit, for different combinations of $\mu_{\rm cm}$ and $\mu_{\rm orb}$.

For $\mu_{\rm cm} = 0.5$ and $\mu_{\rm orb} = 2$, $F_{DF,z}$ takes positive values between 2.4 ($\phi_p = 144°$) and 2.8 orbits ($\phi_p = 290°$). In that range $\dot{z}_p < 0$. The most negative value of $F_{DF,z}$ occurs at 3.12 orbits ($\phi_p = 43°$). Averaged over one orbit, $\langle F_{DF,z}\rangle = -0.06$. On the other hand, $F_{DF,\phi}$ is always negative, that is, extracts angular momentum from the binary, and varies between -1.1 to -0.5, having $\langle F_{DF,\phi}\rangle = -0.7$. This value is similar to the corresponding value in the face-on orbit.

If $\mu_{\rm cm}$ is significantly greater than $\mu_{\rm orb}$ then $\dot{z}_p > 0$ and $F_{DF,z}$ is expected to be always negative. This occurs for

$\mu_{\rm cm} = 2$ and $\mu_{\rm orb} = 0.5$. For those Mach numbers, we find that $\langle F_{DF,z}\rangle = -1.18$, again very similar to the value inferred for the face-on orbit. On the other hand, $F_{DF,\phi}$ reaches a maximum positive value at 0.5 orbits ($\phi_p = 180°$) and then declines to negative values between 0.75 and 1.2 orbits. The average value of $F_{DF,\phi}$ is close to zero.

Finally, we consider a situation where $\mu_{\rm cm} = \mu_{\rm orb} = 1.2$. We see that $F_{DF,z}$ is always negative and its absolute value increases slowly beyond 1.6 orbits. At $\tilde{t} = 9$, $F_{DF,z}$ is about 30% smaller than it is in the face-on case. The azimuthal component of the drag force is positive between 1.35 and 1.65 orbits (ϕ_p between 125° and 165°), and negative otherwise. The average value of $F_{DF,\phi}$ between 1.3 and 2.3 orbits is -0.6, slightly smaller than the corresponding face-on value.

5. DRAG FORCE AND TORQUE ON AN EQUAL-MASS BINARY. FACE-ON CASE

5.1. *Binaries with $\mu_{\rm cm} \neq 0$*

In the last Section, we computed the force acting on a binary component due to the gravitational interaction with its own wake. Here, we wish to estimate (1) the retarding force responsible to decelerate the center of mass of the binary, and (2) the total braking torque on the binary. We shall concentrate on an equal-mass binary in face-on orbit since it represents the simplest situation. We also assume that the two components are on circular orbits with radius R_p about their mutual center of mass.

In the face-on case, the binary is subject to a braking force $2F^{(1)}_{DF,z}$ that decelerates the binary as a whole. Remind that $F^{(1)}_{DF,z}$ is the vertical component of the total force acting on the particle 1, including the contribution of the companion's wake. We have computed $\mathcal{R}_z$ defined as the factor that connects $F^{(1)}_{DF,z}$ with $F_{DF,z}$: $F^{(1)}_{DF,z} = \mathcal{R}_z F_{DF,z}$. For $\mu_{\rm cm} = 0.5$ and $\mu_{\rm orb} = 0.5$, we found numerically that $\mathcal{R}_z = 1.7$. For $\mu_{\rm cm} > 1$, $\mathcal{R}_z$ depends on $\tilde{t}$ and on $r_{\rm min}$. At $\tilde{t} = 9$, our computations indicate that $\mathcal{R}_z = 1.4 - 1.6$ for $\mu_{\rm cm}$ between 1.2 and 4, using $r_{\rm min} = 0.1R_p$. When $t \to \infty$, $\mathcal{R}_z \to 2$ because the z-component of the dynamical friction force is dominated by the far-field wake and, at distances much larger than the binary separation, the far-field wake is almost identical to the wake produced by a point-like object of mass $2M$.

The braking torque is given by:

$$\Gamma = 2R_p F^{(1)}_{DF,\phi}. \tag{24}$$

We may write $F^{(1)}_{DF,\phi} = \mathcal{R}_\phi F_{DF,\phi}$. Values $\mathcal{R}_\phi < 1$ indicate that the wake of the companion reduces the azimuthal drag force. $\mathcal{R}_\phi$ depends on $\mu_{\rm cm}$, $\mu_{\rm orb}$ and $r_{\rm min}$. An exhaustive exploration of the dependence of $\mathcal{R}_\phi$ on these three parameters is beyond the scope of this paper. Roughly, we found that for $r_{\rm min} = 0.1R_p$ and $\mu_{\rm cm} > 1$ or $\mu_{\rm orb} > 2$, $\mathcal{R}_\phi$ lies between 0.57 and 0.7. For $\mu_{\rm cm} < 1$ and $\mu_{\rm orb} < 2$, $\mathcal{R}_\phi$ takes somewhat smaller values. For instance, for $\mu_{\rm cm} = 0.5$ and $\mu_{\rm orb} = 0.5$, $\mathcal{R}_\phi = 0.38$. The $\mathcal{R}_\phi$-value continues decreasing when $\mu_{\rm cm} \to 0$ and $\mu_{\rm orb} \to 0$.

Once $F^{(1)}_{DF,\phi}$ is known, it is possible to derive the temporal evolution of the binary separation. If each component of the binary has mass M, the total orbital angular momentum is $L = \sqrt{GMR_p}$. Thus, $dL/dt = \Gamma$ implies

$$\frac{dR_p}{dt} = 2\sqrt{\frac{R_p}{GM}}\Gamma = 4\sqrt{\frac{R_p^3}{GM}}\mathcal{R}_\phi F_{DF,\phi}. \tag{25}$$

We must just note that we have computed $\mathcal{R}_\phi$ and $F_{DF,\phi}$ as a function of $\mu_{\rm cm}$ and $\mu_{\rm orb}$. In order to integrate Eq. (25), we may use that $\mu_{\rm orb}$ is related to R_p through

$$\mu_{\rm orb} = \frac{1}{2c_\infty}\sqrt{\frac{GM}{R_p}}. \tag{26}$$

In the hypothetical case that $\mathcal{R}_\phi \simeq$const and $|F_{DF,\phi}| \propto \mu_{\rm orb}^{-2}$ then $R_p(t) = R_{p,0}(1 + t/t_{ch})^{-2/3}$, where t_{ch} is a characteristic timescale and $R_{p,0}$ is the initial radius.

5.2. *Binaries with $\mu_{\rm cm} = 0$. Comparison with previous work*

The torque exerted on a binary embedded in a gas was first calculated by Kim et al. (2008), for both subsonic and supersonic orbital motions, assuming that its center of mass is at rest and the two stars are on circular orbits. As already said, we were able to reproduce Kim et al. (2008) results from scratch.

Stahler (2010) also derived analytically the total torque Γ on a "hard" binary (that is, the separation of the binary being smaller than the Bondi radius) in the linear approximation theory. The gravitational potential generated by the binary was expanded in multipoles. In the quadrupole approximation, he found

$$\Gamma = -\frac{16\pi}{15}\frac{\Omega^3}{c_\infty^5}\rho_\infty G^2 I^2, \tag{27}$$

where I is the binary's moment of inertia. For equal-mass binaries, $I = 2MR_p^2$ and $\Omega = V_p/R_p$. Thus,

$$\Gamma = -\frac{64\pi}{15}\rho_\infty \left(\frac{2GM}{c_\infty}\right)^2 R_p \mu_{\rm orb}^3. \tag{28}$$

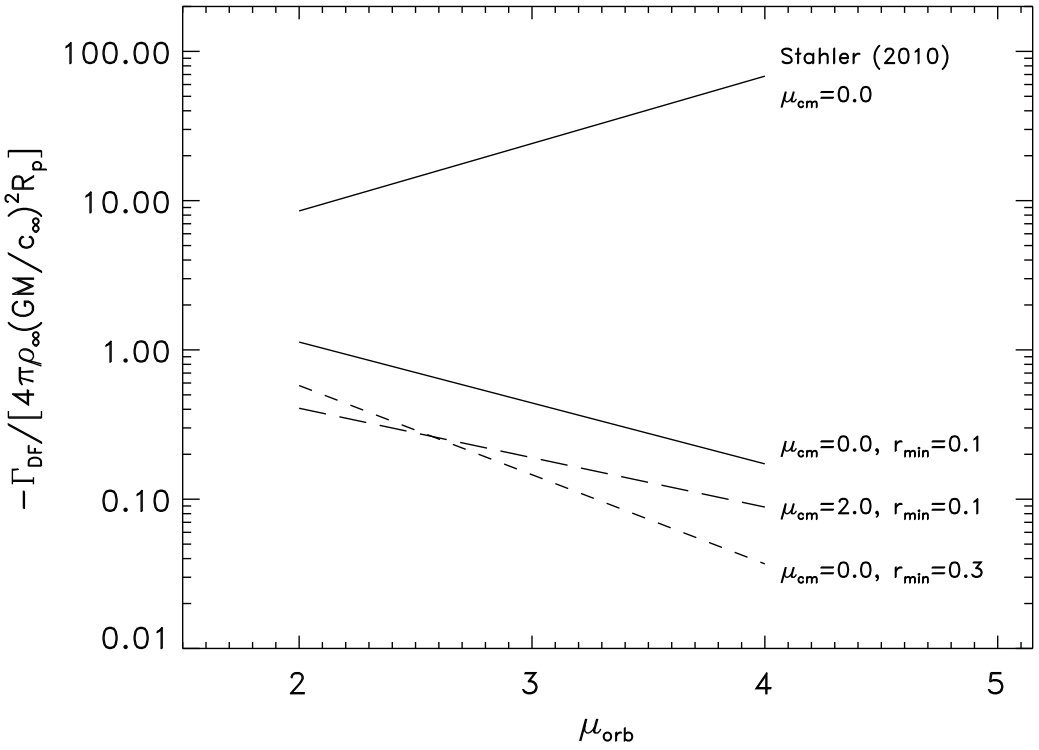

FIG. 13.— Comparison of the torque Γ on an equal-mass binary as a function of $\mu_{\rm orb}$ using Stahler's formula and our semianalytical scheme.

This cubic dependence of Γ with $\mu_{\rm orb}$ is intringuing, especially when the binary is hard and thereby the relative speed of the stars is supersonic respect to the gas. This is in sharp contrast with our findings that the torque decreases with $\mu_{\rm orb}$ in the supersonic case (also Kim & Kim 2007). Figure 13 compares the net torque on an equal-mass binary using our approach (which is identical, but independent, to that used by Kim et al. 2008) and using Stahler (2010) formula. We find clear and significant disagreement with the Stahler (2010) work. For $\mu_{\rm orb} \simeq 4$, the latter formula predicts a torque two orders of magnitude larger than what we got even assuming a rather small value of $0.1R_p$ for $r_{\rm min}$. Note that Stahler's formula has not any explicit dependence on $r_{\rm min}$.

Stahler (2010) carried out a multipole expansion of the gravitational potential created by the binary. In this approach, the perturbed density of the gas can be decomposed as

$$\alpha = \alpha_{-1} + \alpha_{-2} + \alpha_{-3} + ..., \tag{29}$$

where α_{-1} is a term that decays as r^{-1}, α_{-2} decays as r^{-2} and so on. The perturbed density α_{-1} according to Stahler (2010) is

$$\alpha_{-1} = \frac{GM_{\rm tot}}{c_\infty^2 r} - \frac{GI\Omega^2}{c_\infty^4 r}\sin^2\theta\cos 2\left(\Omega t - \frac{\Omega}{c_\infty}r - \phi\right) + \text{higher order terms}, \tag{30}$$

where $M_{\rm tot}$ is the total mass of the binary and θ and ϕ are the polar and azimuthal angles, respectively. The first term on the right-hand-side of Equation (30) corresponds to the monopole contribution of the binary, which produces a spherical and static envelope. We will denote it by α_{-1}^s. The second term on the right-hand-side of Equation (30), which we will refer to it as $\alpha_{-1}^{\rm osc}$, is produced by the quadrupole portion.

The smooth behaviour of the perturbed density distribution described by Equation (30), which oscillates sinusoidally, is in disagreement with the density profile found in our supersonic calculations. As an example, Figure 14 shows the dimensionless perturbed density α, as inferred in our mathematical scheme, through a cut along the positive x-axis for $\mu_{\rm orb} = 4$ (and $\mu_{\rm cm} = 0$), for an equal-mass binary (at $\tilde{t} = 7.5$). We include the wake induced by both components of the binary. The dimensionless static density α_{-1}^s is also drawn. Interestingly, α_{-1}^s traces the density at the center of the spiral arms. We see that, in our computations, $\alpha - \alpha_{-1}^s$ oscillates about zero, but not at all in a sinusoidal way.

The source of the disagreement between our results and Stahler (2010) can be traced back to the multipole expansion, which is not a suitable choice to solve the inhomogenous wave equation (5). Let us rewrite Eq. (30) in terms of

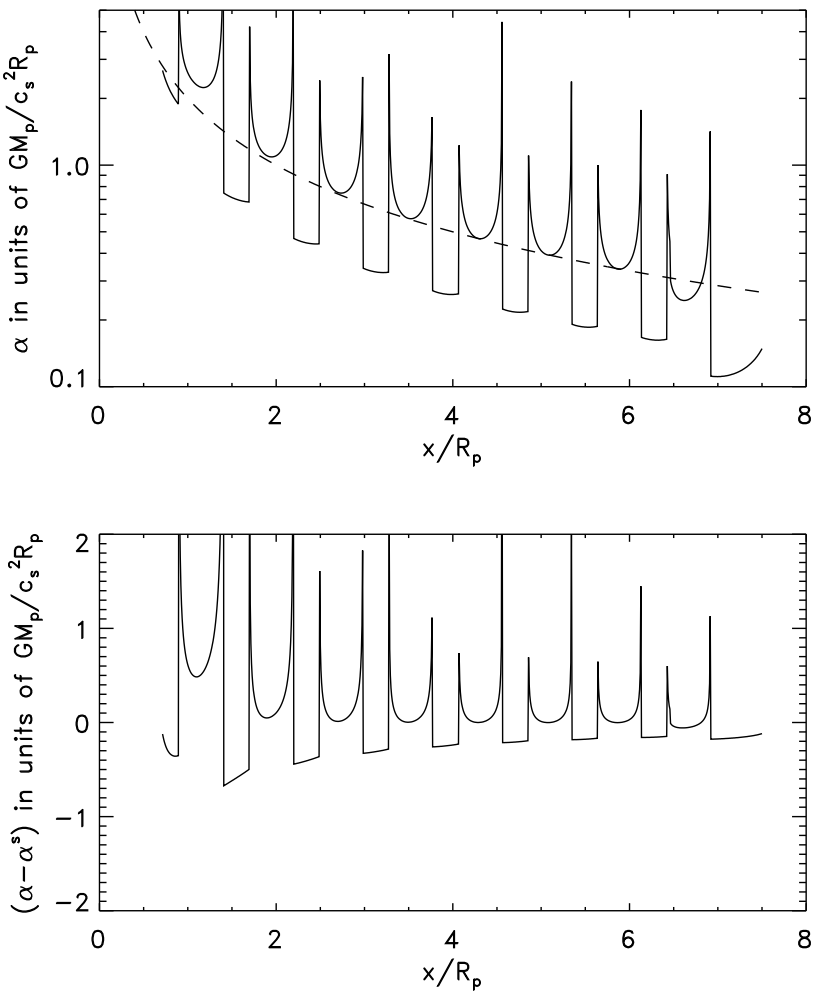

FIG. 14.— Top panel: Density enhancement α (solid line) and monopole contribution $\alpha^s_{\text{-}1}$ (dashed line) along the positive x-axis for an equal-mass binary rotating at $\mu_{\rm orb} = 4$ and $\mu_{\rm cm} = 0$, at $\tilde{t} = 7.5$. Bottom panel: Distribution of $\alpha - \alpha^s_{\text{-}1}$. As the orbital motion is supersonic, the distributions exhibit sharp discontinuities.

$r_{\rm in} \equiv GM_{\rm tot}/(2c^2_\infty)$ and $\Omega_s \equiv c_\infty/R_p$. For equal-mass binaries:

$$\alpha_{\text{-}1} = \frac{2r_{\rm in}}{r}\left[1 - \left(\frac{\Omega}{\Omega_s}\right)^2 + \mathcal{O}\left(\frac{\Omega^4}{\Omega^4_s}\right)\right]. \tag{31}$$

This implies that the multipole expansion is equivalent to a series expansion in powers of Ω/Ω_s. Convergence would require $\Omega \ll \Omega_s$, which implies $\mu_{\rm orb} \ll 1$. Thus, the multipole approach is not valid, at least, for hard binaries. We must warn that the formal solution of the inhomogeneous wave equation given in Equation (6) is an integral over the whole volume. Thus, in order to perform this integral, it is desirable to have a good approximation of $\rho_{\rm ext}$ at every point and not only in the far field, even if $\mu_{\rm orb} \ll 1$.

Korntreff et al. (2012) used Stahler's formula to model the process of the gas-induced orbital decay in hard binaries. They found that orbital decay due to gas-damping can reshape the period distribution of short-period binaries. This conclusion should be revised using more accurate estimates for the torque and including the fact that binaries are in orbits around the center of the star-forming clusters.

6. SUMMARY

There is a variety of astrophysical scenarios where a gravitationally bound system comprised of small gravitational objects, moves relative to the ambient medium. For example, a globular cluster embedded in the gaseous halo of a protogalaxy, a star cluster moving through the disk of a gas-rich galaxy, a binary star traveling within its natal gas cloud, or a binary star embedded in a central stellar cluster subject to a major gas inflow. We have considered the

dynamical friction in the context of a binary system but our analysis may be extended to study other astrophysical situations where the perturbers do not move on rectilinear orbits. In particular, we have provided the mathematical framework to study the gravitational interaction of a binary system with its surrounding gas, when it moves through a uniform, static gaseous background, in linear theory. We have shown how the presence of a binary (instead of a single point-mass) and of the additional component center-of-mass velocity modifies the morphology of the density wake and the nature of the drag force. We have also quantified the internal torques.

Using time-dependent linear perturbation theory, we have developed a semi-analytical scheme to derive the enhanced-density wake created by a binary system. The method is an extension of the work of Kim & Kim (2007). We have first examined the gravitational wake excited in the medium by just one component of the binary. This facilitates comparison with previous studies that consider one single perturber. For simplicity, we have assumed that it is on a circular orbit about the center of mass of the binary. A model is specified with three dimensionless parameters: $\mu_{\rm cm}$ (the Mach number associated with the center of mass), $\mu_{\rm orb}$ (the Mach number of the orbital motion) and i the angle between the orbital axis and $\boldsymbol{V}_{\rm cm}$. We have characterized the wake and computed the drag forces in two cases: when the orbital plane is perpendicular to $\boldsymbol{V}_{\rm cm}$ (face-on case) and when they are parallel (edge-on case).

The morphology of the wake depends on whether the motions are supersonic or subsonic. If both are subsonic (i.e. $\mu_{\rm cm} < 1$ and $\mu_{\rm orb} < 1$), the perturbed density is confined to the sonic sphere centered in the initial position of the perturber. Within the sonic sphere, the perturbed density distribution displays a smooth comma-shape tail along cuts parallel and perpendicular to the orbital plane. When $\mu_{\rm cm} < 1$ and $\mu_{\rm orb} > 1$, the perturber torques the gas and launches spiral trailing waves which transport angular momentum. Finally, when $\mu_{\rm cm} > 1$ and $\mu_{\rm orb} > 1$, the wake displays a very complicated structure, unless $\mu_{\rm cm}$ and $\mu_{\rm orb}$ are very different in magnitude. If $\mu_{\rm cm} \gg \mu_{\rm orb}$, the perturbed density distribution is confined within a deformed Mach cone.

We have computed the drag forces that arise from the gravitational attraction between the perturber and the wake it excites in the ambient medium. We have compared the drag force in the z-direction with that prediced using the Ostriker formula which was derived for a body in rectilinear orbit. If the perturber moves at $\mu_{\rm cm} > 1$, the dynamical friction force in the z-direction is reduced as compared to the rectilinear case because of the loss of gravitational focusing of gas behind the perturber, due to the orbital motion. However, if $\mu_{\rm cm} < 1$, the z-component of the drag force may be larger than in the pure rectilinear case for certain values of $\mu_{\rm orb}$. For instance, for $i = 0$, $\mu_{\rm cm} = 0.5$, $\mu_{\rm orb} = 1.2$ and $r_{\rm min} = 0.1R_p$, the z-component of the drag force is several times larger than it is in the pure rectilinear case ($\mu_{\rm orb} = 0$).

We have also investigated the azimuthal component of the drag force, which causes the binary to lose orbital angular momentum. We have found that Kim & Kim (2007) formula provides reasonable estimates of $F_{DF,\phi}$ as long as $\mu_{\rm cm} < 0.5$ or $\mu_{\rm orb} \gg \mu_{\rm cm}$. In the face-on case, we find that, at a fixed value of $\mu_{\rm orb}$ larger than 1, $F_{DF,\phi}$ decreases with increasing $\mu_{\rm cm}$. As illustration, for $\mu_{\rm orb} = 1.2$, $F_{DF,\phi}$ is a factor of 30 smaller for $\mu_{\rm cm} = 4$ than it is for $\mu_{\rm cm} = 0$. However, for $\mu_{\rm orb} < 1$, $F_{DF,\phi}$ versus $\mu_{\rm cm}$ presents a maximum around $\mu_{\rm cm} \approx 1$. Therefore, it is misleading to think that the translational motion of the center of mass always leads to a decrease in $F_{DF,\phi}$.

Our analysis is especially relevant to understand the gas-induced effects on binary stars when they are still embedded in their parent cloud, or in a central stellar cluster that is undergoing a major inflow of gas (e.g., Davies et al. 2011). Dynamical friction may cause orbital migration of the binary towards the center of the cloud, leading to mass segregation. In addition, the binary can shrink by the tidal torque created by its own wake, reducing its orbital period. We have compared the braking torque acting on an equal-mass binary at rest relative to the ambient medium with that using the analytical formula derived by Stahler (2010). We find that Stahler's formula overestimates the torque. For instance, for $\mu_{\rm orb} = 4$, Stahler's formula overestimates the torque by two orders of magnitude. We conclude that the analysis made by Korntreff et al. (2012) should be revised using the correct magnitude for the torques and including the translational motion of the binaries.

ACKNOWLEDGEMENTS

We would like to thank Ana Hidalgo Gámez and Gonzalo Ares de Parga for useful discussions and for their advice in many aspects. Our special thanks to Nathan Leigh and our anonymous referee for constructive comments on the manuscript. This work was partly supported by CONACyT project 165584 and PAPIIT project IN106212. Raúl O. Chametla acknowledges financial support from a CONACyT scholarship and the grant BEIFI 20141185.

REFERENCES

Amaro-Seoane, P., Sesana, A., Hoffman, L., Benacquista, M., Eichhorn, C., Makino, J., & Spurzem, R. 2010, MNRAS, 402, 2308
Armitage, P. J., & Natarajan, P. 2002, ApJ, 567, L9
Bernal, C. G., & Sánchez-Salcedo, F. J. 2013, ApJ, 775, 72
Bondi, H., & Hoyle, F. 1944, MNRAS, 104, 273
Bonnell, I. A., Clarke, C. J., Bate, M. R., & Pringle, J. E. 2001, MNRAS, 324, 573
Bournaud, F., Elmegreen, B. G., & Elmegreen, D. M. 2007, ApJ, 670, 237
Cantó, J., Raga, A. C., Esquivel, A., & Sánchez-Salcedo, F. J. 2011, MNRAS, 418, 1238
Cantó, J., Esquivel, A., Sánchez-Salcedo, F. J., & Raga, A. C. 2013, ApJ, 762, 21
Chavarría, L., Mardones, D., Garay, G., Escala, A., Bronfman, L, & Lizano, S. 2010, ApJ, 710, 583
Colpi, M. 2014, Space Science Reviews, in press (arXiv:1407.3102)
Davies, M. B., Miller, M. C., & Bellovary, J. M. 2011, ApJ, 740, L42
de Grijs, R., Li, C., Zheng, Y., Deng, L., Hu, Y., Kouwenhoven, M. B. N., & Wicker, J. E. 2013, ApJ, 765, 4
Downing, J. M. B., Benacquista, M. J., Giersz, M., & Spurzem, R. 2010, MNRAS, 407, 1946
Escala, A., Larson, R. B., Coppi, P. S., & Mardones, D. 2004, ApJ, 607, 765
Geller, A. M., de Grijs, R., Li, C., & Hurley, J. R. 2013, ApJ, 779, 30
Heggie, D. C. 1975, MNRAS, 173, 729
Hills, J. G. 1975, AJ, 80, 809

Hoffman, L., & Loeb, A. 2007, MNRAS, 377, 957
Hut, P. 1983, ApJ, 268, 342
Hut, P., McMillan, S., & Romani, R. W. 1992, ApJ, 389, 527
Immeli, A., Samland, M., Gerhard, O., & Westera, P. 2004, A&A, 413, 547
Kim, H., & Kim, W.-T. 2007, ApJ, 665, 432
Kim, H., Kim, W.-T., & Sánchez-Salcedo, F. J. 2008, ApJ, 679, L33
Korntreff, C., Kaczmarek, T., & Pfalzner, S. 2012, A&A, 543, 126
Kulbarni, G., & Loeb, A. 2012, MNRAS, 422, 1306
Leigh, N. W. C., Mastrobuono-Battisti, A., Perets, H. B., & Boker, T. 2014, MNRAS, 441, 919
Li, C., de Grijs, R., & Deng, L. 2013, MNRAS, 436, 1497
Maschberger, Th., Bonnell, I. A., Clarke, C. J., & Moraux, E. 2014, MNRAS, 439, 234
Nordhaus, J., & Blackman, E. G. 2006, MNRAS, 370, 2004
Ostriker, E. C. 1999, ApJ, 513, 252
Ricker, P. M., & Taam, R. R. 2008, ApJ, 672, L41
Sánchez-Salcedo, F. J., & Brandenburg, A. 1999, ApJ, 522, L35
Sánchez-Salcedo, F. J., & Brandenburg, A. 2001, MNRAS, 322, 67
Sigurdsson, S., & Phinney, E. S. 1993, ApJ, 415, 631
Stahler, S. W. 2010, MNRAS, 402, 1758
Taam, R. E., & Sandquist, E. L. 2000, ARA&A, 38, 113

APPENDIX

FACE-ON CASE

Using cylindrical coordinates (R, ϕ, z), where R is the cylindrical radius and ϕ the azimuthal angle, Equation (12), with $i = 0$, is reduced to

$$\mathcal{D}(\boldsymbol{r}, t) = \sum_{\varphi_j} \frac{\mu_{\rm orb}}{|(1-\mu_{\rm cm}^2)\varphi_j - \Omega t - \mu_{\rm orb}^2[\tilde{R}\sin(\varphi_j - \phi) - \lambda\tilde{z}]|} \mathcal{H}\left(\frac{\varphi_j}{\Omega}\right). \tag{A1}$$

Here φ_j are the solutions of the following equation:

$$\mu_{\rm orb}\tilde{d} = -(\varphi - \Omega t), \tag{A2}$$

where

$$\tilde{d}(\varphi; \boldsymbol{r}) = [(\tilde{x} - \cos\varphi)^2 + (\tilde{y} - \sin\varphi)^2 + (\tilde{z} - \lambda\varphi)^2]^{1/2} = [1 + \tilde{R}^2 - 2\tilde{R}\cos(\varphi - \phi) + (\tilde{z} - \lambda\varphi)^2]^{1/2}. \tag{A3}$$

If we define $\omega \equiv \varphi - \phi$, $\eta \equiv \phi - \Omega t$ and $\tilde{a} = (z - V_{\rm cm}t)/R_p$, then

$$\mathcal{D}(\boldsymbol{r}, t) = \sum_{\omega_j} \frac{\mu_{\rm orb}}{|(1-\mu_{\rm cm}^2)(\omega_j + \eta) - \mu_{\rm orb}^2\tilde{R}\sin\omega_j + \mu_{\rm orb}\mu_{\rm cm}\tilde{a}|} \mathcal{H}\left(\frac{\omega_j + \phi}{\Omega}\right), \tag{A4}$$

where ω_j are the solutions of the equation

$$\mu_{\rm orb}\tilde{d}_j = -(\omega_j + \eta), \tag{A5}$$

with

$$\tilde{d}_j(\tilde{R}, \tilde{a}, \eta) = [1 + \tilde{R}^2 - 2\tilde{R}\cos\omega_j + (\tilde{a} - \lambda[\omega_j + \eta])^2]^{1/2}. \tag{A6}$$

The perturbed density distribution created by a perturber in pure circular motion was studied by Kim & Kim (2007). This case correponds to $i = 0$ and $\mu_{\rm cm} = 0$. In that situation, Equations (A4) and (A6) simplify to

$$\mathcal{D}(\boldsymbol{r}, t) = \sum_{\omega_j} \frac{\mu_{\rm orb}}{|\omega_j + \eta - \mu_{\rm orb}^2\tilde{R}\sin\omega_j|} \mathcal{H}\left(\frac{\omega_j + \phi}{\Omega}\right), \tag{A7}$$

and

$$\tilde{d}_j(\tilde{R}, \tilde{z}) = (1 + \tilde{R}^2 - 2\tilde{R}\cos\omega_j + \tilde{z}^2)^{1/2}, \tag{A8}$$

which correspond to Eqs (8) and (6), respectively, in Kim & Kim (2007); just note that they used the letter s instead of η.

EDGE-ON CASE

The edge-on case corresponds to $i = \pi/2$. For this value of the inclination angle, Equation (12) is simplified to

$$\mathcal{D}(\boldsymbol{r}, t) = \sum_{\phi_j} \frac{\mu_{\rm orb}}{|(1-\mu_{\rm cm}^2)\varphi_j - \Omega t - \mu_{\rm orb}^2[\tilde{x}\sin\varphi_j - \tilde{z}(\cos\varphi_j + \lambda) + h(\varphi_j)]|} \mathcal{H}\left(\frac{\varphi_j}{\Omega}\right). \tag{B1}$$

The φ_j-values are solutions of

$$\mu_{\rm orb}\tilde{d}_j = -(\varphi_j - \Omega t), \tag{B2}$$

where

$$\tilde{d}_j(\boldsymbol{r}) = [(\tilde{x} - \cos\varphi_j)^2 + \tilde{y}^2 + (\tilde{z} - \sin\varphi_j - \lambda\varphi_j)^2]^{1/2} \tag{B3}$$

Recall that $\Omega = \mu_{\rm orb}$ in dimensionless units made with R_p and c_∞.

THE LOCATION OF THE ROOTS

In order to not miss any root, we need to constraint the interval that contains the roots. For illustration, we outline the procedure for the case when the orbit is circular and face-on. According to Eqs. (A5) and (A6), the equation for the roots is

$$\mu_{\rm orb}[1+\tilde{R}^2-2\tilde{R}\cos\omega_j+(\tilde{a}-\lambda[\omega_j+\eta])^2]^{1/2}=-(\omega_j+\eta). \tag{C1}$$

The left-hand-side of this equation is positive (or zero), thus $-(\omega_j+\eta)$ must be positive (or zero); this implies that the roots are in the range $\omega\leq-\eta$.

Now we search for a lower bound of the interval. We know that $1+\tilde{R}^2-2R\cos\omega\geq(\tilde{R}-1)^2$, hence

$$\mu_{\rm orb}^2[1+\tilde{R}^2-2\tilde{R}\cos\omega+(\tilde{a}-\lambda[\omega+\eta])^2]\geq\mu_{\rm orb}^2[(\tilde{R}-1)^2+(\tilde{a}-\lambda[\omega+\eta])^2]. \tag{C2}$$

Therefore, it is obvious that those ω's satisfying the inequality

$$\mu_{\rm orb}^2[(\tilde{R}-1)^2+(\tilde{a}-\lambda[\omega+\eta])^2]>(\omega+\eta)^2, \tag{C3}$$

cannot be roots of Equation (C1). This inequatity can be written as

$$(\mu_{\rm cm}^2-1)(\omega+\eta)-2\mu_{\rm cm}\mu_{\rm orb}\tilde{a}(\omega+\eta)+\mu_{\rm orb}^2([\tilde{R}-1]^2+\tilde{a}^2)>0. \tag{C4}$$

Now suppose that $\mu_{\rm cm}>1$, the above inequality implies that, if there are any roots of Equation (C1), they should be located in the interval $\omega_-\leq\omega\leq\omega_+$ with

$$\omega_\pm=\min\left[0,\frac{\mu_{\rm orb}}{\mu_{\rm cm}^2-1}\left(\mu_{\rm cm}\tilde{a}\pm\sqrt{\tilde{a}^2-(\mu_{\rm cm}^2-1)(\tilde{R}-1)^2}\right)\right]-\eta. \tag{C5}$$

We see that when $\tilde{a}^2<(\mu_{\rm cm}^2-1)(\tilde{R}-1)^2$ or $\mu_{\rm cm}\tilde{a}-\sqrt{\tilde{a}^2-(\mu_{\rm cm}^2-1)(\tilde{R}-1)^2}>0$, there is no roots. If $\tilde{a}>0$, the second inequality is $\mu_{\rm cm}^2\tilde{a}^2>\tilde{a}^2-(\mu_{\rm cm}^2-1)(\tilde{R}-1)^2$, or $(\mu_{\rm cm}^2-1)\tilde{a}^2>-(\mu_{\rm cm}^2-1)(\tilde{R}-1)^2$, which always holds. Therefore, the second inequality implies that $\tilde{a}\leq0$ is a necessary condition (not sufficient) to have roots (note that we are studying the case $\mu_{\rm cm}>1$). Putting together the first and the second inequalities, we obtain that the density perturbation is confined to a region having $\tilde{a}\leq0$ and $\tilde{a}\geq-(\mu_{\rm cm}^2-1)^{1/2}(\tilde{R}-1)$. We refer to this region as the "large-scale rear Mach cone", which was mentioned in Section 3.1.

In order to find the interval that contains the roots when $\mu_{\rm cm}<1$, it is useful to start from the following inequality:

$$1+\tilde{R}^2-2\tilde{R}\cos\omega+(\tilde{a}-\lambda[\omega+\eta])^2\leq(\tilde{R}+1)^2+(\tilde{a}-\lambda[\omega+\eta])^2. \tag{C6}$$

Therefore, those ω's satisfying the condition

$$\mu_{\rm orb}^2[(\tilde{R}+1)^2+(\tilde{a}-\lambda[\omega+\eta])^2]<(\omega+\eta)^2, \tag{C7}$$

cannot be roots. After some simple algebra, one can determine the bounded interval $\omega_-\leq\omega\leq\omega_+$ where the roots should lie (when $\mu_{\rm cm}<1$). We find that $\omega_+=-\eta$ and

$$\omega_-=-\frac{\mu_{\rm orb}}{1-\mu_{\rm cm}^2}\left(\mu_{\rm cm}\tilde{a}+\sqrt{\tilde{a}^2+(1-\mu_{\rm cm}^2)(\tilde{R}+1)^2}\right)-\eta. \tag{C8}$$

Contrary to the case $\mu_{\rm cm}>1$, the interval is never null if $\mu_{\rm cm}<1$. In fact, it is easy to show that there is always at least one root for $\mu_{\rm cm}<1$.

We have carried out a similar analysis to constrain the interval to search for the roots in all the cases presented in this paper.